Master Thesis, Department of Geosciences

The Currents in the Outer Oslofjord

An evaluation of measurements and model output

Ole Henrik Botvar

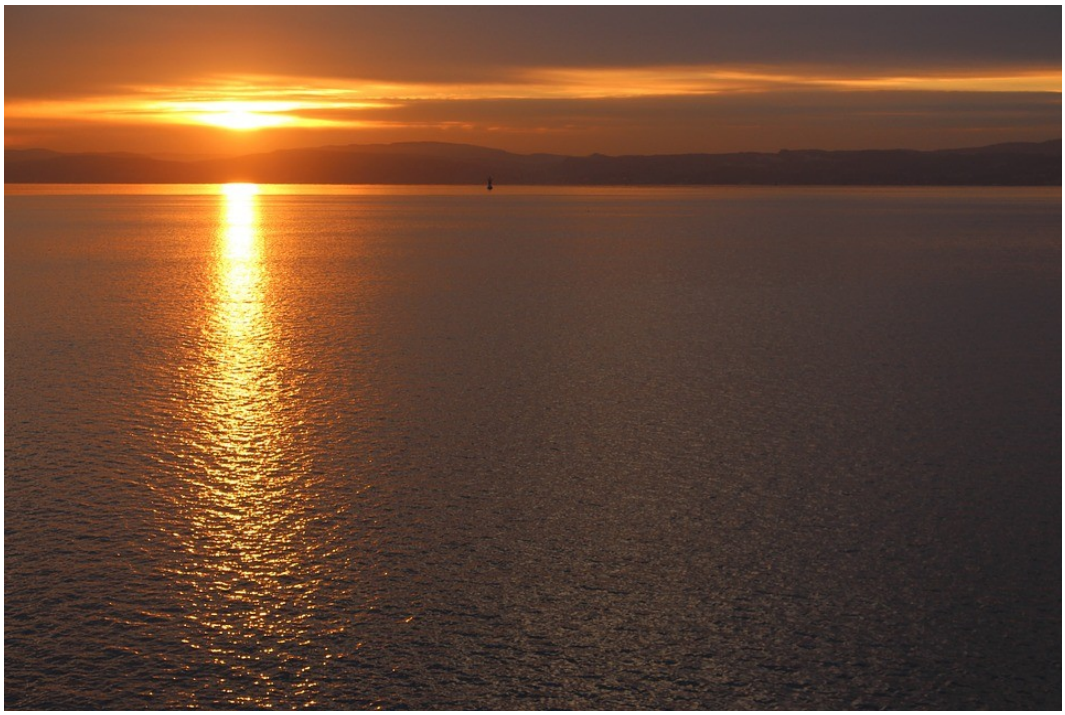

UNIVERSITY OF OSLO

FACULTY OF MATHEMATICS AND NATURAL SCIENCES

The Currents in the Outer Oslofjord

An evaluation of measurements and model output

Ole Henrik Botvar

Master Thesis in Geosciences

Discipline: Meteorology and Oceanography

Department of Geosciences

Faculty of Mathematics and Natural Sciences

University of Oslo

01.06.16

Abstract

This thesis is an investigation of currents in the outer Oslofjord using available tools. Current records and output from the NorKyst-800 model are examined and compared using statistical methods. Internal tidal waves are observed in the Drøbak Strait. Non-tidal frequencies are found to be the most energetic. The strongest currents are found near Bastøy, possibly associated with freshwater flow from Drammenselva. There are often two layers of current, of which the uppermost layer could be wind-driven and the second layer could be associated with the estuarine circulation. Topographic waves seem to exist near the bottom. Integral time scales are about one day. There is a weak clockwise turning of current with depth near the surface. In general, the current tends to go along-fjord. The currents are statistically Gaussian. Similarities to baroclinic modes with rough bottom are found. There are quite a few differences between the data and the model output, mostly due to the model bathymetry. Some differences, like the absence of bottom-strengthened currents, could be associated with a low vertical resolution. It is concluded that more current sensors recording over a longer time period, in addition to salinity and temperature loggers, are needed in order to fully understand the dynamics in the outer Oslofjord.

Acknowledgements

Firstly, I want to thank my main supervisor Joseph Henry LaCasce for his supervision during the work with the thesis, in particular with respect to the structure and the statistical analysis. Furthermore, I want to thank my co-supervisor Andre Staalstrøm for inspiring discussions and help with the data. Moreover, I am thankful to the crew onboard R/V Trygve Braarud, who enabled the collecting of data in the outer Oslofjord. I also want to thank Lars Petter Røed and Jan-Erik Weber for coming with useful input during the work with the thesis.

Thanks to those of you who read through my thesis; Eirin, Kristoffer, Kjersti, Nils-Otto and Per Gunnar. I am grateful for the help you gave me in a hectic period. Moreover, I want to thank my friends and family for encouragement and support. Lastly, I am very grateful for the help from Kjell when my laptop broke down. Without this help, I could have lost many days of work.

Contents

Chapter 1

Introduction

1.1 The Oslofjord

The Oslofjord is a roughly 120 km long fjord stretching from Færder lighthouse via Oslo Harbour to Ås (Baalsrud and Magnusson, 1990). It is an important recreational area for the population around it. Leisure boat driving and fishing are popular activities in the fjord. Furthermore, there is a lot of ship traffic by cargo ships, cruise ships, public transport boats and fishing trawlers (Baalsrud and Magnusson, 2002).

The Oslofjord is not formed like a typical fjord, because it is part of a geological rift (Staalstrøm et al., 2012). The Drøbak Sill splits the fjord into its inner and outer part, of which only the outer part is studied here. The inner fjord has a maximum width of about 7 km before it narrows down to about 1 km in the Drøbak Strait, see Figure 1.1. Its width extends to about 18 km in the Breiangen basin. Near Bastøy, the width decreases to about 10 km before the fjord opens up towards Skagerrak.

The fjord has two large fjord arms, namely the Bunnefjord (from Oslo to Ås) and the Drammenfjord (from Breiangen to Drammen). There are many islands in the fjord, of which the largest one is Jeløya (close to Moss) with an area of about 19.7 km^2. Håøya and Bastøy are also fairly large.

The depth of the inner fjord peaks at about 150 m. It decreases to 20 m at the Drøbak Sill, before it goes back to about 150 m in the rest of the Drøbak basin. A sill of 100 m isolates this basin from the Breiangen basin, which is also around 150 m at most. Further south, after another sill of approximately 100 m, we find the Bastøy basin, which is about 300 m deep at most. The two southernmost basins in the fjord are the Rauer basin and the Hvaler deep, of which the latter is the deepest basin with a maximum depth of 450 m.

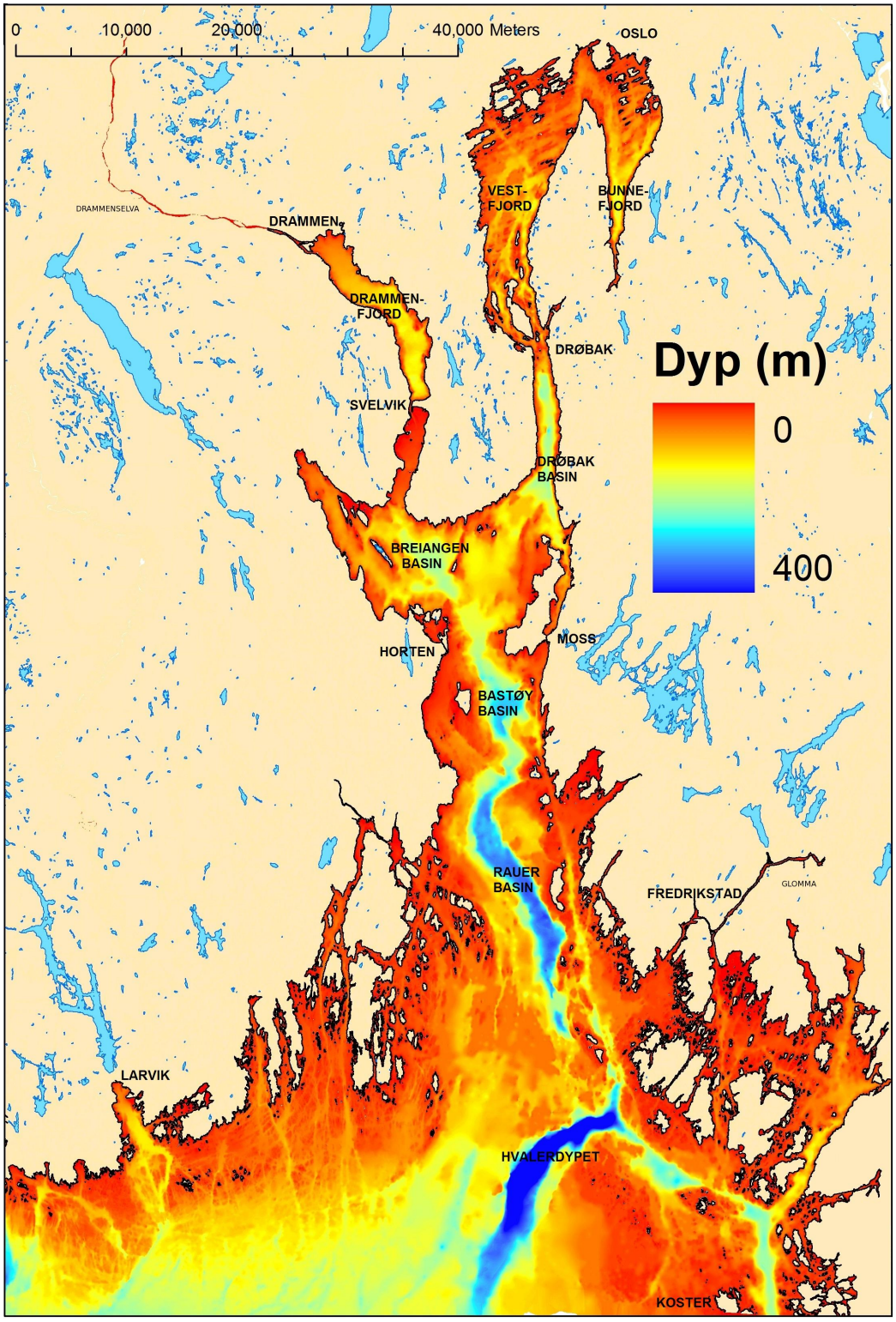

Figure 1.1: A map of the Oslofjord with the names of its basins. Adapted from Staalstrøm and Ghaffari (2015).

The surface wind over the Oslofjord follows certain patterns. In the wintertime it is typically northerly. It peaks in strength in January and is usually weaker than 3 (3.3 ms^{-1}) on the Beaufort scale. In the summer, the wind has a more variable direction. South-southeasterly winds are most frequent, but northerly winds are also common. The summer winds are strongly modified by sea and land breeze on warm days, and they are strongest in the afternoon. They do typically not exceed 3 on the Beaufort scale either (Gade, 1968). Climate change is not shown to alter these wind patterns, see Thaulow and Faafeng (2014).

The main freshwater supply comes from Glomma (annual average 720 m^3s^{-1}) and Drammenselva (annual average 330 m^3s^{-1}). Only a small part comes from the rivers in the Inner Oslofjord (Akerselva, Lysakerelva etc., annual average 27 m^3s^{-1}). Because of this, the brackish surface current often flows inward rather than outward. This is not a typical fjord circulation (Gade, 1968). It occurs particularly in early summer, when Glomma and Drammenselva have large water fluxes and the spring flood in the small rivers are over. It also happens on warm days in which the evaporation in the inner fjord is larger than the runoff from local rivers (Baalsrud and Magnusson, 2002).

The earliest oceanographic studies of the Oslofjord consider its hydrography, that is, its water mass characteristics (Hjort and Gran, 1900; Braarud and Ruud, 1937). The water masses in the fjord are a mixture of Skagerrak water and local water affected by rivers (Baalsrud and Magnusson, 2002). In the Skagerrak the North Atlantic Current, the Jylland Current and the relatively fresh Baltic Current meets (Rodhe, 1996). Thus, the Skagerrak contains a mixture of many different water masses. The most important mechanisms exchanging water masses between the fjord and the Skagerrak are the estuarine circulation and the wind driven circulation (Gade, 1968). For instance, Klinck et al. (1981) finds that along-shore winds outside the fjord (i.e. near the Skagerrak) can initiate flooding of (in this case mostly) Baltic water.

Despite being somewhat affected by Skagerrak, most of the water in the fjord is locally formed. Numerous eddies contribute to this by increasing the mean residence time (Dahl et al., 1990). These eddies are mainly generated through tides and cyclones and anticyclones (Gade, 1968). The average water level variation caused by tides is about 28 cm. It can be larger if there is a strong high or low pressure system over the fjord. In extreme cases the water level can change by several meters over a period of 5-6 hours (Baalsrud and Magnusson, 2002). The dominant tidal frequency in the fjord is the M_2 component, with a mean amplitude of about 14 cm (Aas, 2011, p. 112). With an estimated fjord surface area of 550m^2 north of Bastøy, this gives an

approximated tidal water flux near Bastøy of about $7000 m^3 s^{-1}$. Stigebrandt (1979) gives observational evidence for internal waves of tidal origin in the fjord. Staalstrøm et al. (2012) finds that due to these internal waves, the diffusivity near the Drøbak Sill is more than four times larger than in the rest of the fjord. This, in turn, is proven to affect the frequency of deepwater renewals.

One of the earliest studies of surface current patterns in the Oslofjord is done by Johannessen (1967). In this study, current crosses are used to investigate the currents in the Vestfjord (see Figure 1.1). It is found that the currents are mainly going northwards and southwards, that is, along the fjord axis. Furthermore, the surface currents respond relatively swiftly to wind events, typically within one or two days.

The Norwegian Institute of Water Research (NIVA) investigates measurements of surface currents in the outer Oslofjord and compare them with a reduced gravity model (Dahl and Hackett, 1988; Skåtun and Røed, 1988; Dahl et al., 1990; Røed et al., 1990; Røed and Skåtun, 1990). The surface currents are found to be baroclinic and directed mainly southwards. Furthermore, four central surface eddy areas are detected between Breiangen and Færder, occasionally joining to one big cyclonic eddy. The typical time scale for the motion is found to be on the order of 4-6 days.

Other examples of model studies in the Oslofjord include Svendsen et al. (1995), Grinde (2011) and Isachsen (2014). The latter compares output from the NorKyst-800 model in the fjord to a model with higher spatial resolution. It is found that in open regions, the two models give similar results. However, particle trajectories are different and the model with higher resolution resolves smaller, stronger eddies.

1.2 An overview of this study

The main focus in this thesis is the examination of current records in the outer Oslofjord. There are several examples of studies which have a similar objective, e.g. for the Gulf Stream at 68° west (Hall, 1986). A subgoal is to find out how well the NorKyst-800 model, provided from the Norwegian Meteorological Institute (NMI), reproduces the currents. We will compare the current records to model output for the same period. Examples of earlier studies of this kind is the one by NIVA mentioned earlier and LaCasce and Engedahl (2005) and LaCasce (2005b) for the western Norwegian shelf and slope.

We look for typical frequencies in the motion, for instance to see what kind of tidal regime is found in the fjord. Are the diurnal or semidiurnal tides

most important? Exactly which tidal frequencies dominate? Furthermore, we are interested in the non-tidal frequencies. What is the typical frequency of motion when the tides are removed?

We will also look for general characteristics of the flow. At which depths and locations is the flow strongest? Is the current going mainly along or across the isobaths? When does a strong current occur, and how long does it typically last? What is the typical time scales for motion in the fjord, that is, how fast does the current change?

In addition, we will check if there are particular patterns in the flow direction. Is it going mostly northwards or eastwards, for instance? Does the current mainly follow the bathymetry or the coastline? Does the direction change with depth or with location? We will also check the degree of randomness of the current strength. Are there any statistically significant current anomalies, or are the currents more or less random?

Moreover, the vertical variation of current is considered. Is it strongest near the surface or further down? How does it evolve with depth? Does it decay or increase towards the bottom? How many times does it change sign with depth?

When it comes to the model, we want to know how well it reconstructs the flow, as already mentioned. Does the model resolve small eddies in the current? Are the directions approximately correct? Are there any differences in agreement between grid points close to the coast and grid points in the middle of the fjord?

Several statistical measures are calculated in order to answer these questions. Power spectral densities (PSDs) are used to find dominant frequencies. Tidal currents are removed with the use of harmonic analysis and Butterworth filtering. Typical time scales are found via autocorrelation functions. Variance ellipses are applied to find the typical flow directions and PDFs are used to find extreme values. Lastly, empirical orthogonal functions are calculated to examine the vertical structure of the flow.

What do we expect to find? Because Stigebrandt (1979) finds evidence for internal tides, we expect to find it in these data as well. Furthermore, we expect time scales of about 4-6 days, just like in the joint model and measurement study from NIVA. Moreover, the currents should follow the fjord-axis, just like Johannessen (1967) finds in the inner fjord, if the dynamics are similar.

There are several motivations for this study. Firstly, because few measurements are taken in the outer Oslofjord, it is interesting to see how the currents behave there. If the model validation is promising, it can be used to further investigate the dynamics of the fjord, by for instance considering larger areas or longer time periods. Experimenting with different driving

forces could also be helpful. A better physical understanding of the fjord dynamics is advantageous, for instance due to all the ship traffic. The model could make forecasts of the fjord currents as well. This could be useful in the event of an oil spill like Godafoss (Broström et al., 2011) or a man over board situation. In addition, if one knows the typical current strengths, tension on constructions in the fjord can be estimated.

This thesis is arranged as follows. The next chapter discusses background theory. After this, the measurement campaign is described, followed by an outline of the NorKyst-800 model. Then the statistical tools, such as the variance ellipses, are explained. Next, the results from using these tools are described for the measurements (Chapter 6) and for the model (Chapter 7). The last chapter is a summary of these results.

Chapter 2

Theory

This chapter discusses some topics that are relevant for the interpretation of the results. First, there is a section on tides (Section 2.1). Next, baroclinic modes are considered (Section 2.2). We then finish off the chapter with a discussion on topographic waves (Section 2.3).

2.1 Tidal currents

Tidal currents are induced by the sum of gravitational forces from the Sun and the Moon on the Earth. These forces can be described as a sum of a finite set of sinusoids at specific frequencies. The frequencies are linear combinations of six fundamental frequencies arising from planetary motion (Pawlowicz et al., 2002). Among these frequencies the most important ones are the lunar day (the rotation of the Earth about its rotation axis), the lunar month (the rotation of the Moon around the Earth) and the tropical year (the orbit time of the Earth around the Sun). Linear combinations of these give the typical frequencies of tidal currents, such as the M_2 (lunar semidiurnal) component of 12.42 hours and the K_1 (lunisolar diurnal) component of 23.93 hours.

Tidal dynamics are not always linear, that is, the ocean does not necessarily respond with the same frequencies as the forcing (Pawlowicz et al., 2002). This is the case if the tidal waves are of comparable height to the ocean depth. Then shallow-water tidal components are introduced, which have higher frequencies than the standard tidal components. These frequencies can also be determined from linear combinations of the fundamental frequencies (Aas, 2011).

2.2 Baroclinic modes

The depth profile of the velocity in the ocean can be decomposed into a linear combination of a set of functions called modes. The modes can be obtained from the Navier-Stokes equations with the following assumptions:

- The topographic gradient is weak
- The Rossby number is small
- The beta-effect is small

Assumption number one means that there can be no steep slopes in the sea floor. Thus we must have that $\frac{|h|}{D_0} \ll 1$, where D_0 is a reference depth and $h(x, y)$ is the local deviation from D_0. x and y are the zonal and meridional coordinates, respectively.

The second assumption requires that the local acceleration is much less than the Coriolis force. Mathematically, we must have that $\frac{U}{fL_{xy}} \ll 1$, where U is the order of magnitude of the current, $f = 2\Omega \sin(\theta)$ is the Coriolis parameter ($\Omega = 7.27 \times 10^{-5}\text{s}^{-1}$ is the Earth's rotation rate and θ is the latitude) and L_{xy} is the typical length scale of motion.

The lateral variation in the Coriolis force must be small for the last assumption to be fulfilled. If we simplify the Coriolis parameter to $f = f_0 + \beta y$, we must have $\mid \beta y \mid \ll f_0$. In this formula, f_0 is the mean Coriolis parameter over a smaller area (e.g. for the Oslofjord) and β is a constant parameter. One may write $\beta = \frac{2\Omega}{a}\cos(\theta)$, where a is the radius of the Earth. In practice, this assumption means that we can only consider a limited meridional range (LaCasce, 2012).

Through these assumptions we obtain the quasi-geostrophic potential vorticity (QGPV) equation, which upon linearization takes the form

$$\left[\nabla^2\psi + \left(\frac{f^2}{N^2}\psi_z\right)_z\right]_t + \beta\psi_x = 0 \tag{2.1}$$

It is an equation for the streamfunction $\psi = \frac{p}{\rho f}$, where p is pressure and ρ is density. ψ relates to the velocity vector $\boldsymbol{u} = u\boldsymbol{i} + v\boldsymbol{j} + w\boldsymbol{k}$ as $\boldsymbol{u} = \boldsymbol{k} \cdot \nabla\psi$. Subscripts mean "differentiated with respect to". z is the vertical position, t is the time and N is the Brunt-Väisälä frequency $N^2 = -\frac{g}{\rho}\rho_z$, where g is the acceleration of gravity. The modes are found by assuming a wave solution of 2.1 with a depth-varying factor, to compensate for the stratification: $\psi = \phi(z)\hat{\phi}e^{i(kx+ly-\omega t)}$. Here k and l are the wave numbers in the x and y direction, respectively, and ω is the frequency (LaCasce, 2012).

It is common practice to assume flat surfaces at the upper and lower boundary, which can be expressed as $w = \phi_z = 0$ at $z = 0$ and $z = -H$,

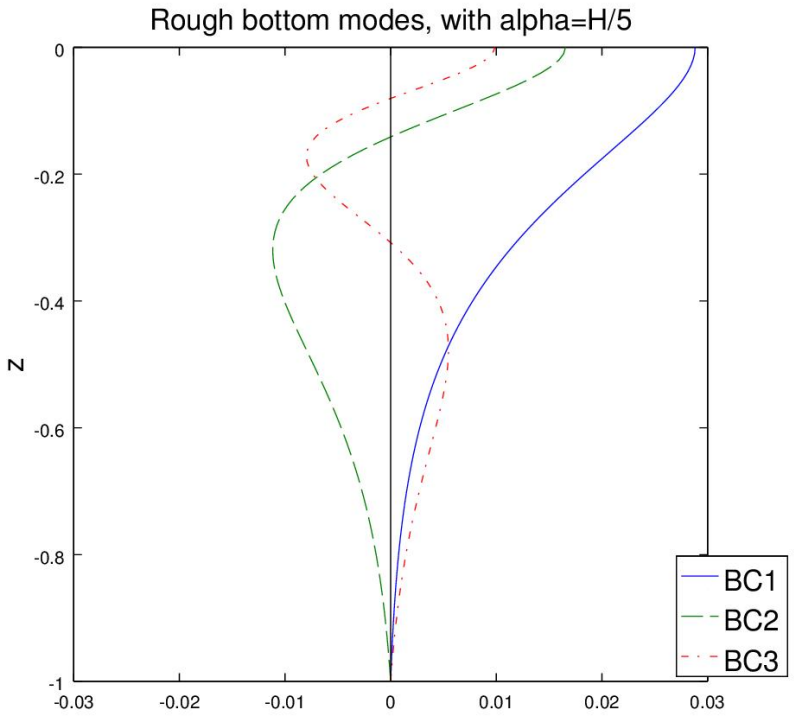

Figure 2.1: Figure showing the baroclinic modes (abbreviated to BC). Here $\alpha = H/5$. The depth z is normalized.

where H is the ocean depth (Wunsch, 1997). In the outer Oslofjord, however, it is better to take the ocean floor to be steep or rough, i.e. put u and v equal to zero at $z = -H$ instead of w (Pedlosky, 1987; LaCasce, 2012). This is because in relatively shallow waters (the Oslofjord is usually less than 200 m deep), bottom friction has a larger relative influence on the flow. This affects the vertical structure. Another reason for saying that u and v are small, as opposed to w, is that all the measurements have been taken on places with steep bathymetry (although the inclination is still less than 1%, see Figure 3.1).

The simplest modes are found by assuming that the stratification is constant. A more realistic solution is obtained by saying that the stratification is exponential, i.e. $N^2 = N_0^2 e^{z/\alpha}$, where N_0 is the stratification at the surface and α is a constant scaling parameter. Figure 2.1 shows how the baroclinic rough bottom modes look for exponential stratification. We can see that the first mode (BC1) has no zero crossings and decays fairly rapidly towards zero, whereas the higher modes have more zero crossings.

2.3 Topographic waves

A topographic slope also supports low frequency wave solutions like those in the previous section. To see this, consider again the linearized QGPV equation 2.1. If we assume that the mean flow is negligible, put $\beta = 0$ (that is, the area of interest is fairly small so that $f \approx f_0$) and assume no stratification (constant N), we get

$$\nabla^2 \psi_t + \frac{f_0^2}{N^2} \psi_{zzt} = 0 \tag{2.2}$$

We assume a linear bottom topography $H = D_0 - ky$ (k is constant) and, like before, a wave solution of the type $\psi = \phi(z)\hat{\phi} e^{i(kx+ly-\omega t)}$. With this, we find that the shallow water is to the right of the propagation direction in the Northern Hemisphere. The waves have an exponentially decaying amplitude from the sea floor, given by

$$\phi(z) = Ae^{-N\kappa z/|f_0|} \tag{2.3}$$

Here A is the wave amplitude at the sea floor and $\kappa = \sqrt{k^2 + l^2}$. From this formula, it is possible to estimate the size of topographic waves if they exist. The vertical extent of the waves can be estimated from the e-folding scale, $L_z = \frac{|f_0|}{N\kappa} = \frac{|f_0|\lambda}{2\pi N}$, where λ is the wavelength of the waves. Thus, if one reformulates this equation, the wavelength can be estimated as $\lambda = \frac{2\pi N}{|f_0|} L_z$, assuming L_z is known.

The most common approach for observing topographic waves is to look for spatial correlations (with some lag) between measurements along the same isobaths. LaCasce (2005b) did this for data from the west coast of Norway, but did not find much evidence for topographic waves, at least not for separations down to 10 km. A simpler way of spotting topographic waves is by looking for intensification in the flow near the bottom (Equation 2.3). Topographic waves have been observed many places, for instance near oceanic shelves where the sea floor is steep (Smith and Schwing, 1991; Moseidjord et al., 1999; Wåhlin, 2002).

Chapter 3

Data

3.1 Field work

Current sensors were deployed in the outer Oslofjord from the 16th September to the 25th November 2014. A map of the study area with all the sensor locations and the nearest weather station is shown in Figure 3.1. In Table 3.1, the exact measuring period, the location and the water depth for each sensor is specified. Some of the instruments stopped recording before the 25th November, due to loss of battery power.

Station number	Name of location	Start time	End time	Total depth [m]	Latitude Longitude
1	Småskjær	17/9 14:00	25/11 7:20	20	59.350124 10.497661
2	Laksetrappa	17/9 14:00	25/11 7:50	75	59.343452 10.581023
3	Botnegrunnen	19/9 14:00	18/11 21:30	96	59.352375 10.626822
4	Evje	16/9 14:00	25/11 8:40	64	59.363182 10.653576
5	Brenntangen	18/9 14:00	25/11 13:40	54	59.581803 10.646087
6	Filtvedt	17/9 21:20	9/11 11:50	153	59.582064 10.627372

Table 3.1: Table showing the recording times, the local ocean depth and the location for each sensor.

The data collecting process was a collaboration between NIVA, Statnett,

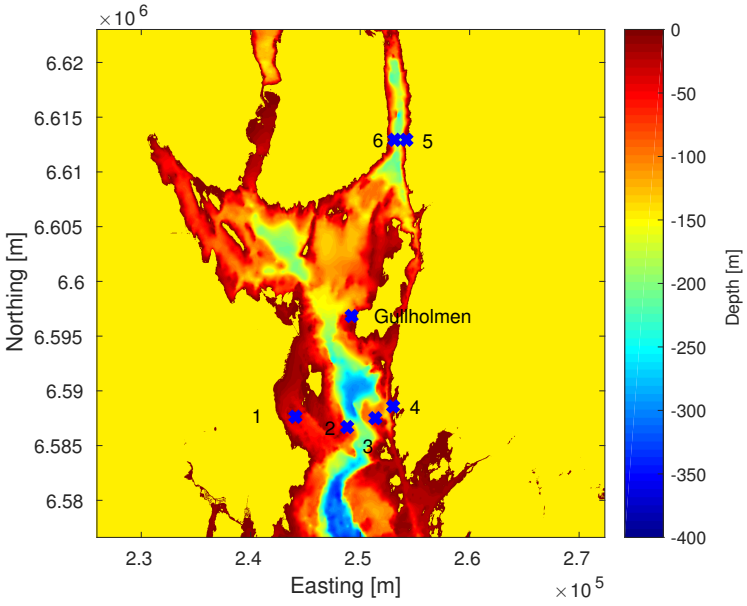

Figure 3.1: Map showing all the sensor locations (red crosses) and the location of the nearest operational weather station (Gullholmen).

the University of Oslo (UiO) and Akvaplan NIVA. The research vessel R/V Trygve Braarud was used for the field work. The sensor positions were chosen from Statnett's high-resolution terrain model.

As we can see in Figure 3.1, two sensors were installed in the southern end of the Drøbak Strait (station 5 "Brenntangen" and station 6 "Filtvedt" in the Figure). The bathymetry is steep on both sides of this channel-like area. Statnett is planning on installing power cables on the sea floor approximately where these two sensors are located.

Furthermore, four sensors were placed slightly south of Bastøy (see Figure 3.1). Along this cross-section, cables have been installed at the sea floor. Some of these stations have been given names based on their bathymetry. For instance, station 1 is located close to some tiny skerries, hence the station name "Småskjær" (in English: "Small skerry"). Station 2, on the other hand, is located in an area with staircase-like bathymetry and is thus called "Laksetrappa" (in English: "Salmon staircase"). Station 3 "Botnegrunnen" is situated on a fairly steep slope in the east-west direction and station 4 "Evje" is hidden inside a small bay with a decent slope. There is a deep channel in the middle of the cross-section.

The wind at Gullholmen during the measuring period is shown in Figure 3.2. The location of this weather station can be found in Figure 3.1. The time resolution for these measurements is 6 hours. We can see that the wind

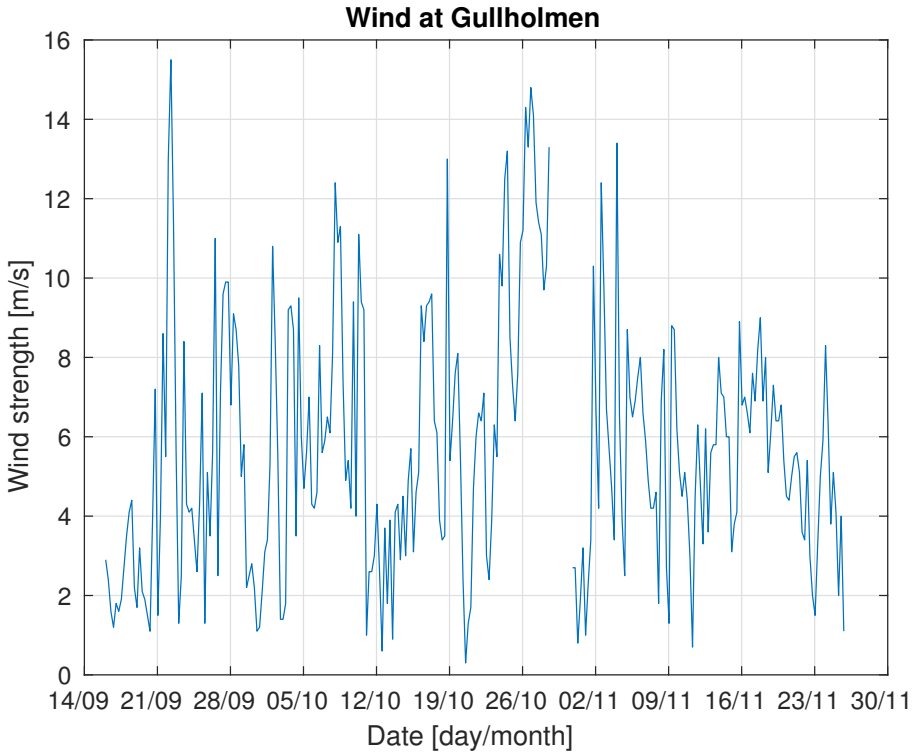

Figure 3.2: Wind speed measured at the weather station at Gullholmen from 16th September to 25th November.

ranges from almost calm conditions (0.3 ms^{-1}) to about 16 ms^{-1} (moderate gale). Normally, it is between 2 ms^{-1} and 9 ms^{-1}.

3.2 Current profilers

Two types of Acoustic Doppler Current Profilers (ADCP) were used for the data acquisition; the Nortek Aquadopp and the Nortek Continental. They measure three-dimensional current in an adjustable number of depths within the water column. See Table 3.2 for the depths chosen for each station. The instruments send beams in three different directions, each oriented 25° from the vertical centre line. These beams are reflected from particles in the water column. The current is calculated from usage of the Doppler principle. The built-in magnetic compass and the tilt sensor helps to calculate the current in the $x-$, $y-$ and $z-$ direction.

The resolution was chosen so that the precision never was worse than 2 cms^{-1} (see Table 3.2). A better precision requires a decrease in vertical res-

St. no.	Instrument	Res. [m]	Min. [m]	Max. [m]	Freq. [Hz]	Avg. [s]	Prec. [cms^{-1}]
1	Aquadopp600 AQP1531	2	4.5	16.5	600	180	1.8
2	Aquadopp400 AQP4689	3	14	71	400	220	1.7
3	Continental WAV6117	7	13	83	190	110	1.4
4	Aquadopp400 AQP2931	3	9	60	400	240	1.6
5	Aquadopp400 AQP5608	3	8	50	400	240	1.6
6	Continental CNL6037	5	16	146	190	220	1.4

Table 3.2: Instrument specifications. St. no = station number, res. = resolution (vertical), min. = minimum depth, max. = maximum depth, freq. = frequency, avg. = averaging period and prec. = precision

olution. In order to have a large vertical range, the frequency of beams must be low. As we can see in Table 3.2, the frequency, given by the instrument hardware, ranges from 190 Hz to 600 Hz.

The instruments give a new reading every 10 minutes. The readings are averages of the signal recorded during an averaging period within these 10 minutes. A longer averaging period gives a better precision, but it also consumes more battery. Thus, choosing the averaging period is a balance between precision and battery power needs (in this case battery power was needed for two months and about 8-9 days). From the requirement of a 2 cms^{-1} precision, averaging periods in the range of 2-4 minutes had to be used, depending on the vertical precision (see Table 3.2).

The current sensors were moored to the seafloor with stones. In order to stabilize the instruments during strong currents, floats were attached to the upper part of the mooring system. Maximum tilt angles for the current profilers ranged from 1.6° to 15.27° (Staalstrøm and Ghaffari, 2014). Acoustic release mechanisms were used to recover the instruments.

Chapter 4

The NorKyst-800 model

NorKyst-800 is a numerical model which covers the entire Norwegian coast. The model was developed at the Institute of Marine Research (IMR) in cooperation with NMI and NIVA. The grid is rectangular and contains 2600×900 cells in the horizontal. Like the name suggests each cell is 800×800 m. There are 17 depth levels, and the vertical resolution is highest near the surface. The time step is one hour, which enables the model to resolve the most important topographical features and dynamical processes along the Norwegian coast (Asplin, 2011). In this thesis, only daily mean output is used.

The model gives the state of the sea, that is, the ocean temperature, the salinity, the sea level and the current in real time, a few days into the future and up to several decades backwards. It utilizes Arakawa C grids. This means that the free surface, the density and active/passive tracers are calculated in the middle of each grid cell, while the east-west velocity and the north-south velocity is calculated on the east/west and the north/south edges.

There are many applications for this, of which some have already been mentioned specificly for the Oslofjord in Section 1.2. In a broader sense, the Norwegian coast is complex and presents many challenges for the offshore industry. For instance, companies building and maintaining hydro power stations and oil rigs can benefit from knowing the typical ocean condition at some particular locations. Furthermore, the model can be used to check the effects of for instance eutrophication near the coast. Another useful application is to get an overview of the coastal environment (Albretsen, 2011; Asplin, 2011).

The model requires initial conditions for current, salinity and temperature. In addition comes the boundary conditions, which include bathymetry, atmospheric forcing and river runoff. Bathymetry with original resolution of 50 m taken from Statens Kartverk Sjø has been modified to fit to the model

grid. Open boundary conditions are taken from the partially overlapping ROMS application Nordic4km, which is a 4 km resolution model covering the Norwegian Waters (Shchepetkin and McWilliams, 2005). The atmospheric forcing consists of daily (00, 06, 12, 18 UTC) analysis of wind, temperature, pressure, cloud cover and humidity. Furthermore, 12 hour accumulated fields of precipitation and long wave radiation and 24 hour accumulated fields for short wave radiation are utilized. The runoff input is based on modeled discharge by the Norwegian Water Resources and Energy Directorate (NVE) from a total of 249 catchment areas along the Norwegian and Swedish coast (Beldring et al., 2003; Albretsen, 2011).

Chapter 5

Methods

In this chapter, all the different methods used to analyze the measurements and the model output are presented. First, two different techniques for removing tidal frequencies are described. This is followed by a discussion of PSDs which are used to find the typical (tidal and non-tidal) frequencies of motion. After this, a method of finding typical time scales (the autocorrelation function) is outlined. Variance ellipses, which are used to find direction patterns, are explained afterwards. Then comes an account of PDFs, applied to detect for instance extreme flows. The last topic in the chapter is the empirical orthogonal functions. These are used to look at the vertical profile of current.

5.1 De-tiding of the current

The current signal can be split into a high-frequency (periods shorter than about a day) and a low-frequency component. The tidal signal is contained in the former. In this thesis, much emphasis is given to the low-frequency signal. Two different methods for de-tiding the measurements are applied: The harmonic analysis (Pawlowicz et al., 2002) and the Butterworth filter (Roberts and Roberts, 1978).

5.1.1 Harmonic analysis

Harmonic analysis has been applied to estimate the tidal currents. The tide $\widetilde{u}$ can be written as a sum of harmonic components (see also 2.1):

$$\widetilde{u} = \sum_i U_i \cos(\omega_i t - \theta_i) \tag{5.1}$$

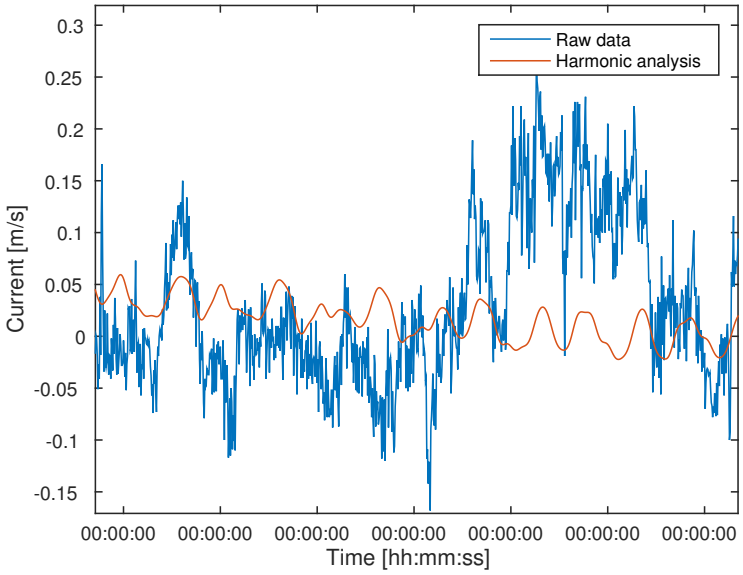

Figure 5.1: Plots of raw current data (blue curve) and harmonic analysis (red curve) for station 1's zonal flow component at 4.5 m depth, from the 17th to the 24th of September.

where U_i, ω_i and θ_i are the amplitudes, frequencies and phases of tidal component i, respectively. Once these constants are found, $\widetilde{u}$ is simply subtracted from the flow to give the non-tidal current. This is sometimes an efficient technique, because it exploits the deterministic character of the tidal signal.

The method has some drawbacks, however. For instance, in order to resolve all the possible tidal frequencies, 18.6 years of time series is needed. This is because the smallest fundamental frequency, which is the lunar orbit tilt, has this period. For shorter time series, this problem can be solved by introducing nodal corrections. These are small temporal variations in the tidal constituents. However, if the record length is smaller than one year, such as here, this correction can be ignored.

On the other hand, if the record is much shorter than one year, the frequency resolution becomes quite low. Then it is hard to distinguish between different tidal frequencies. This might be the case with the data presented here, see Figure 5.1. We can see that the raw data (blue curve) and the harmonic analysis (red curve) do not follow each other very well. Although the non-tidal signal also is important, this might indicate that the frequency resolution for the analysis is too low.

Another issue with the method is that it is not so easy to check the origin of each frequency. Sometimes the method might give output coming from the non-tidal broad-spectrum variability, and this is not easy to detect.

Furthermore, the method does not account for temporal variations in the tidal signal. Since we are looking at a fjord, the tide is nonstationary. There are seasonal variations in the tidal response, caused by for instance seasonal salinity changes.

In addition, non-linear effects may occur. These can not be captured by harmonic analysis (Pawlowicz et al., 2002). As mentioned earlier (Section 2.1), non-linear effects tend to show up when the tidal wave has an amplitude comparable to the ocean depth. The typical tidal variation in the Oslofjord is about 20 cm (Section 1.1), while the lowest depth is about 20 m, which is a factor 100 larger. Thus, non-linear effects are probably of minor concern in this case.

The `MATLAB` function `t_tide` is used to determine the harmonic signal. This function accounts for 45 astronomical and up to 101 shallow water components in the harmonic analysis. The default choice is to include the 24 most important shallow water components, which is done here, in addition to shallow water component M_{10}. The tidal response model in `t_tide` is

$$c(t) = b_0 + b_1 t + \sum_{k=1}^{K} (a_k e^{i\sigma_k t} + a_{-k} e^{-i\sigma_k t}) \tag{5.2}$$

where c is the tidal response and the σ_k are frequencies. The first two terms represent a possible offset and an optionally added drift current, respectively. Without these terms the equation resembles Equation 5.1, except that it uses complex numbers. The coefficients $a = [b_0, b_1, a_1, a_{-1}, a_2, a_{-2}, ...a_{-K}]$ are determined through a least squares fit to the observations $o = [o(t_1), ...o(t_M)]$, where M is the length of the time series.

5.1.2 Butterworth filtering

As we have seen, the removal of harmonic components may not always remove the full tidal signal. In order to make it less likely to have tidal remnants in the data, a low-pass filter has been used. A low-pass filter is a filter where frequencies above a certain threshold are removed, leaving the lower frequencies unaffected.

A good low-pass filter should have a sharp cutoff at the maximum frequency, have a sensible response to sudden peaks in the data, have a minimal phase shift, be as flat as possible in the passband and require little computer time (Roberts and Roberts, 1978). There are many filters that score well on the first four requirements, e.g. the Cosine-Lanczos filter, the Gaussian filter and the ideal filter. The Butterworth filter, however, retains these advantages without the high computational cost present in the three former

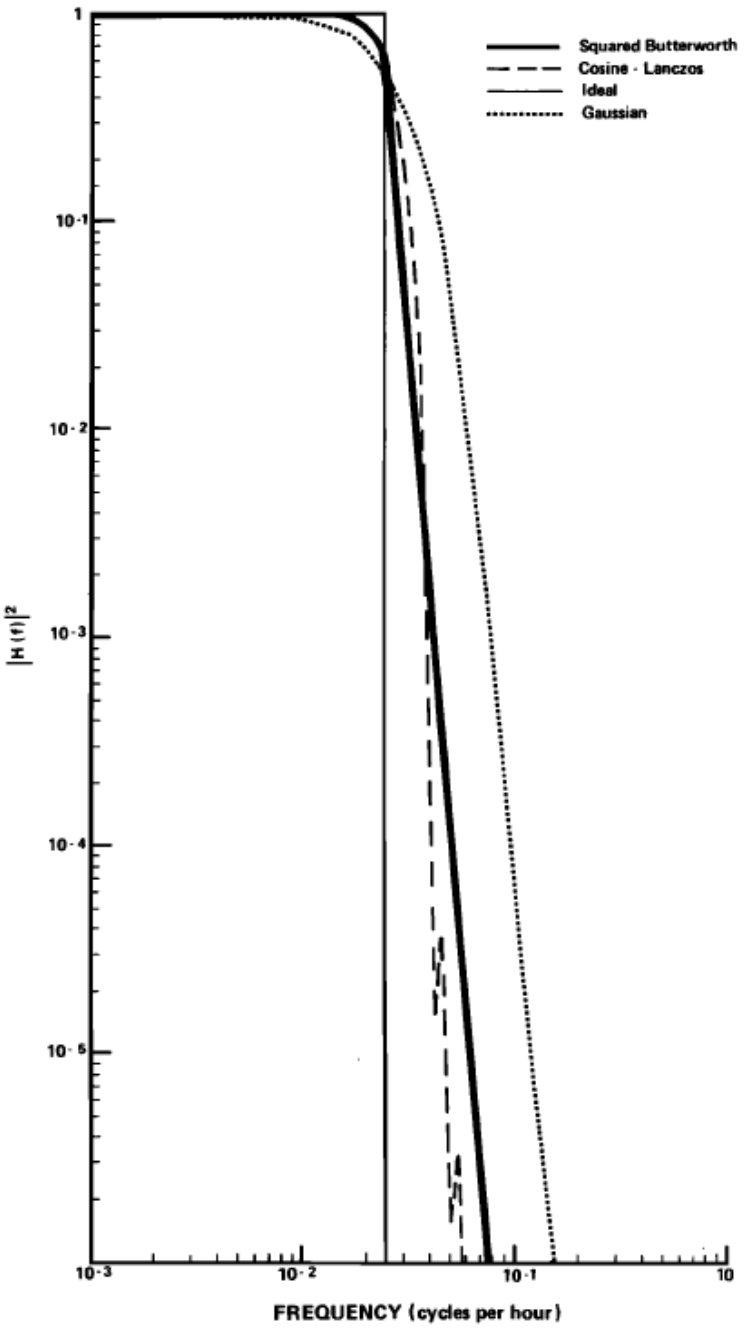

Fig. 1. Power gain functions for four low-pass filters with cutoff frequency at 1/40 hours. The cosine-Lanczos and Gaussian filters each were given 60 weights.

Figure 5.2: A comparison of the squared Butterworth filter, the Cosine-Lanczos filter, the Ideal filter and the Gaussian filter. Figure adapted from Roberts and Roberts (1978).

filters.

For a discrete system, the Butterworth filter is defined as the square of its transform function H_B:

$$|H_B(i\omega)|^2 = |1 + \frac{\tan(\omega T/2)}{\tan(\omega_C T/2)}|^{-2n} \tag{5.3}$$

Here T is the sampling time and n is the order of the filter. ω_C is the cutoff frequency. In this work, $n = 4$ and $\omega_C = 1/25$. Roberts and Roberts (1978) showed that an order of 4 removes the tides sufficiently. A higher order makes the filter more prone to roundoff errors. A cutoff frequency of 1/25 should be sufficient for removing all the dirunal and semidiurnal tides, but as we will see (Section 6.3), there seems to be some remnants of short period signals in the filtered data.

The Butterworth filter equation (Equation 5.3) is compared to the other mentioned filters in Figure 5.2. We can see that the ideal filter has the sharpest cutoff and is flattest in the passband. However, this results in a worse response to spurious signal changes, and this is not present in the Butterworth filter. The Butterworth filter also scores fairly well on cutoff sharpness and passband flatness.

In order to apply the filter to the data, the filter coefficients $\{c_n\}$ and $\{d_n\}$, which are the poles of 5.3, are calculated. These are fed into the filter equation $c_1 O_m = d_1 o_m + d_2 o_{m-1} + ... + d_{n_d+1} o_{m-n_d} - c - 2O_{m-1} - ... - c_{n_c+1} O_{m-n_c}$, which is solved in `MATLAB`. Here O_m is the filtered time series at time t_m. n_c and n_d are the feedback and feedforward filter orders, respectively. We can see that the filter is recursive, i.e. past values are needed as input. Unfortunately, a phase shift will occur, but this can be avoided if one filters forwards and then backwards. Then the power gain function will be the square of the original, and this is what is shown in Figure 5.2.

5.2 Power spectral densities

One purpose of the PSD estimate is to find dominant frequencies in a signal. That is the purpose it has served in this thesis.

The PSD can be expressed as:

$$\hat{P}(\omega) = \frac{\mathrm{d}t}{M} |\sum_{m=0}^{M-1} o_m e^{-i2\pi\omega m}|^2 \tag{5.4}$$

$\hat{P}$ is called a periodogram of the signal and $\mathrm{d}t$ is the time step. The sum over frequencies of the spectrum is equal to the total (horizontal) kinetic energy,

and thus the spectrum says something about the importance of different frequencies. In order to calculate the Fourier transform mentioned above, one has to assume that the motion is stationary. In this case, stationarity means that the mean and variance does not change significantly within neighbouring time intervals.

If the time series is relatively long, that is, spanning several years, one can divide it into several segments with some overlap and apply a window to each segment. These windows typically have decreasing values near the extremities for smooth overlap between them. For instance, a Hamming window is used in Welch's method (Welch, 1967) while in Thompson's multitaper method (Thomson, 2000) Slepian windows are used. The advantage with overlaps is that the spectral estimate gets smoother. However, for short time series like the ones presented here it makes more sense to consider the periodogram itself without overlaps.

In this thesis, the PSDs are normalised. This eases the comparison of different spectra in the same graph. Moreover, they are plotted in a semilogarithmic coordinate system so that the high frequencies are better resolved. Vertical lines representing different tidal constituents are plotted in the same graphs for comparison.

5.3 Autocorrelation functions

In order to find typical time scales for the currents, the autocorrelation function

$$r(\tau) = \frac{\overline{o'(t)o'(t+\tau)}}{\overline{o'(t)o'(t)}} \tag{5.5}$$

is calculated. Here, overbars are temporal block averages and $o' = o - \bar{o}$. From r, the integral time scale can be obtained. This time scale is important for three reasons: Firstly, it is the time scale over which perturbations remain correlated. Secondly, it is proportional to the inverse of the peak frequency in the PSD. Thirdly, it must be well resolved by the averaging period, which is about 2-4 minutes for the measurements. For the model output, it is one day.

It is common to determine the integral time scale by assuming that the autocorrelation function decays exponentially with respect to time (see e.g. Roberts and Roberts (1978); LaCasce (2005b)). That is, one assumes that $r(t_j) \propto e^{-\frac{t_j}{T}}$ where T is the integral time scale, also called the e-folding time scale (Lenschow et al., 1994; LaCasce and Engedahl, 2005). The least

squares method can be applied to fit the autocorrelation to an exponential. If the e-folding time for instance is 3 days, this usually means that a typical fluctuation in the current lasts for about 3 days before it is decorrelated.

We will see that the autocorrelation functions presented here do not fit so well to exponentials (Section 6.3). Therefore, another method for determining the integral time scale is also used, namely the convergence value of the cumulative sum of the autocorrelation function multiplied by dt (Lenschow et al., 1994; LaCasce et al., 2014).

5.4 Variance ellipses

The purpose with variance ellipses is to find the dominant directions of variability for a dataset. Like the name suggests, one gets information about the variance as well.

In order to calculate variance ellipses, one first needs the covariance matrix

$$\mathcal{C}_{\mathbf{u}} = \begin{bmatrix} \sigma_u^2 & \overline{u'v'} \\ \overline{u'v'} & \sigma_v^2 \end{bmatrix} \tag{5.6}$$

where u and v are the east-west and the north-south components of the velocity vector, respectively. The σ are variances in the u- and v-direction, and $\overline{u'v'}$ is the covariance. The eigenvectors and eigenvalues of the covariance matrix define the orientation and the size of the ellipse, respectively. The major axis of the ellipse goes along the eigenvector with the largest eigenvalue. This eigenvalue corresponds to half the length of the major axis, say, a. Similarly, the minor axis has the length of the smallest eigenvalue (e.g. b) and the direction of the corresponding eigenvector. The coefficients a and b also correspond to the variances in the direction of the eigenvectors.

The equation for the ellipse becomes

$$\left(\frac{X}{a}\right)^2 + \left(\frac{Y}{b}\right)^2 = s \tag{5.7}$$

where X and Y are the coordinates of the ellipse and s works as a scaling. By usage of the chi-square cumulative distribution (Lilliefors, 1967), s can be chosen so that a given percentage of data points can fit inside the ellipse. These values can be looked up in tables. For instance, in order to fit 95% of the data points into the ellipse, which we do here, s has to be 5.991.

5.5 Probability density functions

As we have seen, variance ellipses only capture variability within +/− a standard deviation from the mean. Probability density functions (PDF), on the other hand, also show data which is several standard deviations away from the mean.

An empirical PDF is a histogram where the data is sorted into normalized bins. It can be approximated by a distribution function. An example of such a distribution function is the Gaussian distribution, which is given by

$$p(o) = \frac{1}{\sigma_o\sqrt{2\pi}} e^{-\frac{(o-\bar{o})^2}{2\sigma_o^2}} \tag{5.8}$$

Here σ_o is the standard deviation of the variable o.

A PDF might differ significantly from the Gaussian distribution. If that is the case, it shows that there are significant extreme values in the data. Examples of PDF plots can be found in LaCasce (2005b). In this article, some PDFs have peaks at +/− 4 standard deviations away from the mean. This shows that there are persistent flow features in the dataset. A similar situation is found in LaCasce (2005a).

The Kolmogorov-Smirnov test is a way of comparing two different PDFs. In this thesis, we compare PDFs from the current meters with Gaussian distributions. If $s(o)$ is the sample cumulative distribution and $f(o)$ is the Gaussian distribution, the value of $B = \max|f(o) - s(o)|$ determines if the test is rejected or not. If it is rejected, the data is not Gaussian, or normally distributed. The critical value of B for different amounts of data are obtained from Monte Carlo calculations (Lilliefors, 1967). They can be looked up in tables.

5.6 Empirical orthogonal functions

So far we have looked at ways to describe temporal variability, current strength and current direction. Empirical orthogonal functions (EOFs), on the other hand, can be used to characterize spatial (here: vertical) variation of data. The EOFs resemble the dynamical modes in Section 2.2, see also (Wunsch, 1997).

In order to compute EOFs, data from each station must be organized into a matrix $F = [\underline{f}_1 ... \underline{f}_m ... \underline{f}_M]$. Each column vector $\underline{f}_m$ is a depth profile of the current at time t_m. The covariance matrix $R = M^{-1}FF^T$ is then calculated and the eigenvalues and eigenvectors of R are found through solving $RC = C\Lambda$. (Notice that this covariance matrix is organized differently from

that in Section 5.4.) Here, $C = [\underline{v}_1 \ldots \underline{v}_j \ldots \underline{v}_J]$ contains the eigenvectors of R and $\Lambda = \text{diag}(\lambda_1 \ldots \lambda_j \ldots \lambda_J)$ contains the corresponding eigenvalues of R (J is the number of depth levels recorded). Each eigenvector is an EOF. Its corresponding eigenvalue equals the fraction of total variance in R explained by that particular eigenvector. In other words, $\underline{v}_j$ has a relative resemblance of λ_j to all the observation vectors $\underline{f}$ simultaneously (Kutzbach, 1967; Bjornsson and Venegas, 1997).

Chapter 6

Results and discussion

In this chapter, the results of applying the methods in Chapter 5 to the data in Chapter 3 is presented, starting off with power spectral densities. The currents are projected onto components along and across the isobaths. This is because it makes it easier to detect phenomena which are related to topography.

6.1 Power spectral densities

The PSD shows how much variance that is contained in each frequency. In other words, it states which frequencies are most important in the motion. One reason for calculating PSDs is to find out whether the current is dominated by tides or not. Furthermore, one can see which tidal or non-tidal frequencies are most significant.

The PSDs for the lowermost recording level at station 1 is shown in Figure 6.1. We can see that there is a peak near the M_2 frequency. There are also peaks at harmonic overtides of the M_2 component. This is also seen at station 2 and 6.

For the stations in the Drøbak Strait, the M_2 peak is clearest near the surface, i.e. at about 15-20 m depth. It is most dominant in the component across the topography. As mentioned earlier, internal waves of tidal origin (M_2) propagate from the Drøbak Sill, which is also about 20 m deep. The stations near Bastøy, which are further away from the Drøbak Sill, have a stronger M_2 signal at about 50-60 m depth. The sharpest stratification gradients are found at these depths.

Station 4 is the only station where the M_2 component is not the dominant tidal signal. This station is slightly sheltered inside a small bay. Instead, there are significant contributions from O_1, K_1 and S_2. These dominate at

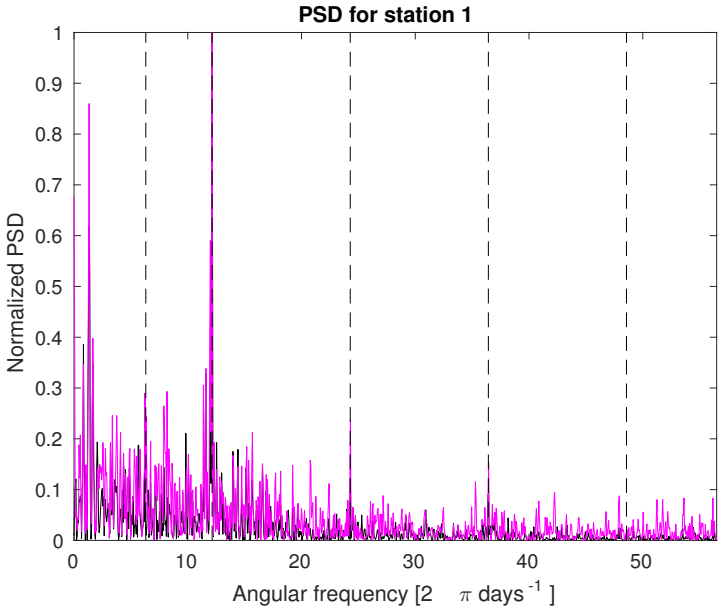

Figure 6.1: PSDs for station 1 for the parallel flow (purple) and the normal flow (black). The recording closest to the bottom has been chosen. Vertical lines representing different tidal constituents are plotted, in order to find out which ones that dominate. From left to right: K_1, M_2, M_4, M_6 and M_8

different depths. Some of them are more important in the parallel flow than in the normal flow, and vice versa.

The largest peaks in the PSDs are fairly often sub-tidal. They have a period ranging from 2 days to about the duration of the time series. Moreover, they are often multiples of each other. For instance, a period of 7.3 days is often accompanied by a period of 14.6 days. The record length is fairly short, and this might affect the frequency spectrum. Sub-tidal frequencies are normally most dominant near the surface. They are clearest in the flow normal to the contours in the Drøbak Strait.

6.2 Hovmöller diagrams

From this section onwards, only the low-frequency (de-tided) currents are studied. Hovmöller diagrams are useful for giving an overview of the temporal and spatial (here depth) variability. They can show whether the flow is strongest along or across the topography, and how strong it is in each of these components. In addition, one can see how the current fluctuates with time, for instance how fast it changes. One can also see how long strong flow

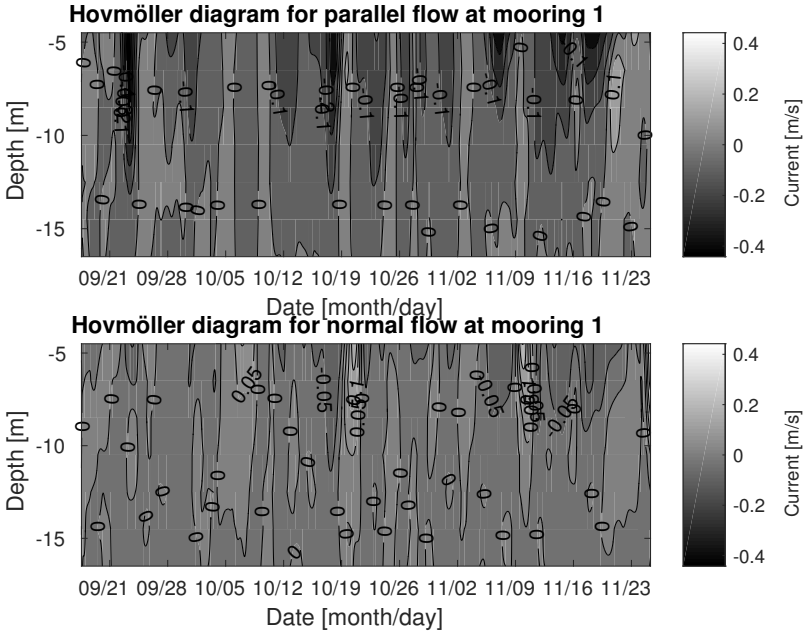

Figure 6.2: Hovmöller diagram of parallel and normal flow at station 1.

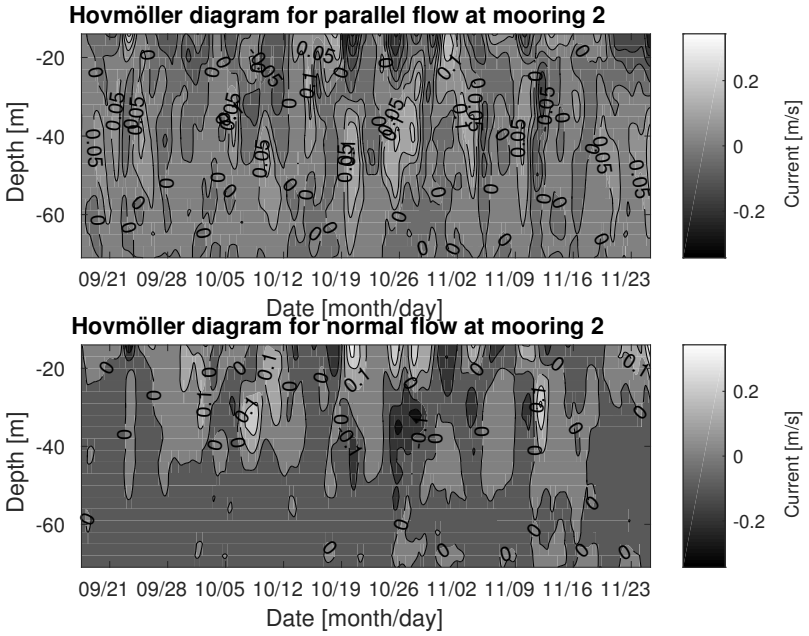

Figure 6.3: Hovmöller diagram of parallel and normal flow at station 2.

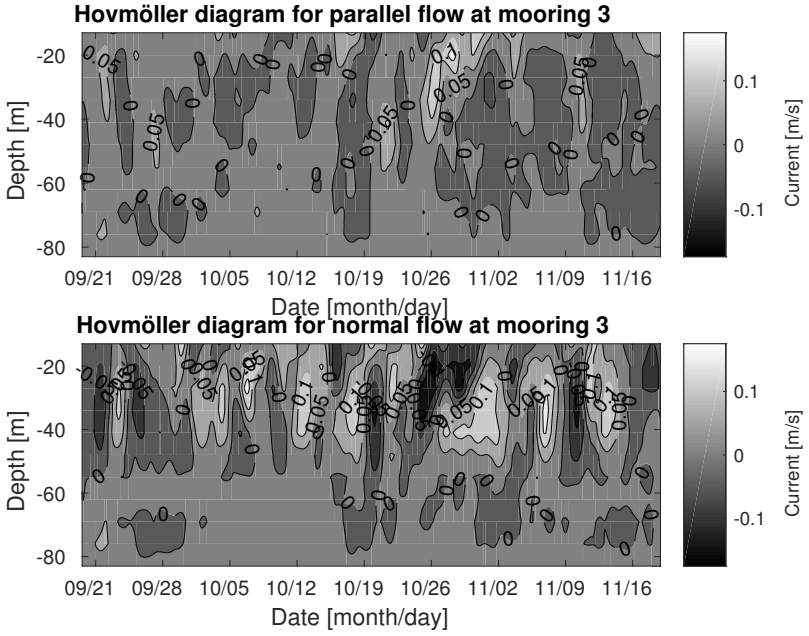

Figure 6.4: Hovmöller diagram of parallel and normal flow at station 3.

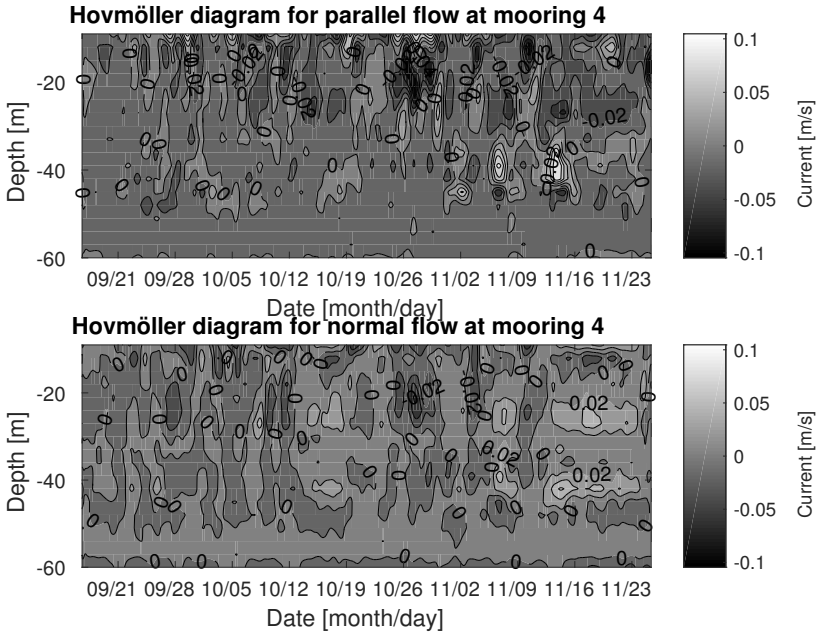

Figure 6.5: Hovmöller diagram of parallel and normal flow at station 4.

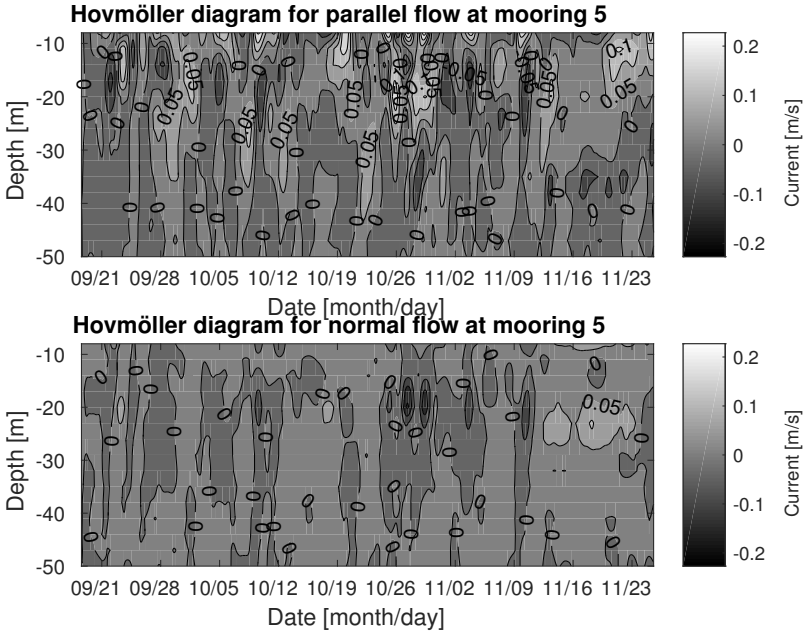

Figure 6.6: Hovmöller diagram of parallel and normal flow at station 5.

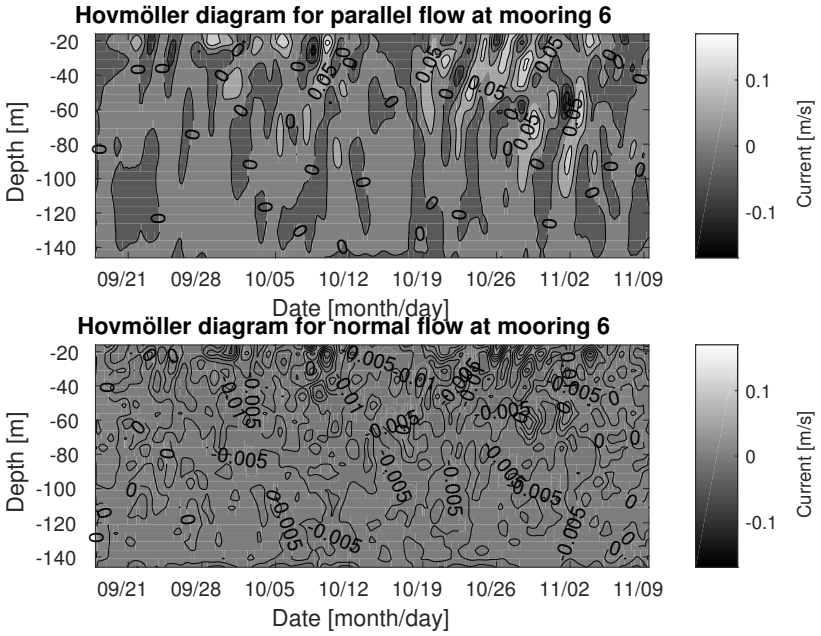

Figure 6.7: Hovmöller diagram of parallel and normal flow at station 6.

events typically last. Is it one day or one week? The diagrams may also show whether there are vertical layers in the flow where it is generally stronger or weaker. For instance, it may show whether the flow is bottom intensified, or if there is a surface intensification. Furthermore, although not done here, one can be able to tell how fast a flow event spreads vertically. More specificly, one can estimate the vertical diffusion.

Figure 6.2, 6.3, 6.4, 6.5, 6.6 and 6.7 shows Hovmöller diagrams of the along and across current measured at each station. The strongest currents are found at station 1, which is the shallowest station (only 20 m deep). The currents are up to 0.5 ms^{-1}. This is also the only station with measurements closer than 10 m from the surface. Station 2 also has quite significant currents, about 0.4 ms^{-1} at most. These moorings are both located near the Drammensfjord, from which a strong brackish flow is expected due to Drammenselva. The currents at the other stations are typically on the order of 0.1-0.2 ms^{-1}. The weakest flow is found at station 4, which is closest to the coastline.

The flow is usually strongest along the isobaths. The strongest dominance of the parallel flow compared to the normal flow is found at the stations in the Drøbak Strait, especially at station 6. In this area the fjord is narrow, and it is formed like a channel. At station 2 the perpendicular component dominates instead. Here, the isobaths are approximately perpendicular to the fjord 'axis'.

Normally, the flow seems to have two distinct layers. The exception is station 1, where the flow events are always near the surface. As mentioned earlier, this station is shallow. Occasionally, one can see three different layers. This is typically at the deepest stations.

The uppermost layer near the surface can be distinguished from its short-lived current events. The peaks decay in strength down to about 10-12 m, and sometimes even further. They last for about 1-3 days, and they tend to appear simultaneously at all the stations. The frequency of occurrence is about 2-4 times per month. Both wind forcing and brackish water currents can generate such events. A visual comparison is done between the surface events and the wind strength at Gullholmen (Figure 3.2). Sometimes, a strong wind event is followed by a current maximum, while on other occasions there is no apparent response in the surface current. The water flux from Drammenselva is also compared to the surface currents, but with little agreement.

Below the surface layer, the flow often goes in the opposite direction. This pattern resembles that of estuarine circulation. Sometimes, the flow in this intermediate layer is stronger than the near-surface flow. Unfortunately, there are no measurements from the uppermost 5-10 m, except at station 1.

The currents in the third layer, when it exists, are typically reversed with respect to the currents in the second layer. The events in the intermediate layers have variable vertical extents of about 5-20 m.

Near the bottom the flow weakens, and it decays more rapidly across the topography. At some stations, however, in particular station 3 and 4, the flow intensifies near the bottom instead. This phenomenon often appears in the cross-isobath flow. At these two stations, the isobaths are at right angles to the fjord orientation, which we will see is the general flow direction. Topographic waves are often excited by such bathymetry. If topographic waves exist in the area, their wavelength can be estimated by knowing their approximate vertical extent and the stratification (see Section 2.3). The vertical extent can be estimated visually. For for station 4's component normal to the topography, it is about 3 m. The stratification, estimated from CTD measurements in the vicinity, is found to be in the range 0.015-0.025 s^{-1}. Thus, the estimated wavelength is 2.3-3.8 km.

6.3 Autocorrelation functions

The main reason for calculating autocorrelation functions is to see how fast the currents change with time. It gives us the typical time scale for motion. For instance, one can find out whether the time scale changes with depth or with location.

As mentioned earlier, autocorrelation functions are often compared to exponentials. However, the autocorrelation functions in this study do not resemble exponential functions (see Figure 6.8). Recall that the time series is relatively short (about two months). The function also has a lot of wiggles at large values of τ. E-folding (integral) time scales have been estimated as the time delay for which normalized autocorrelation functions are reduced to $1/e$, see Table 6.1 and

Station 1			Station 2			Station 3		
z	τ_N	τ_P	z	τ_N	τ_P	z	τ_N	τ_P
4.5	1.1	1.3	17	1.3	1.3	13	1.2	1.2
6.5	1.0	1.1	26	1.3	0.9	20	1.3	1.5
8.5	0.9	0.9	35	1.5	0.9	27	1.1	1.2
10.5	0.8	0.9	44	1.2	0.9	41	1.3	1.1
12.5	0.7	0.9	53	1.2	1.0	55	0.7	1.0
14.5	0.7	0.8	62	1.0	1.0	69	2.5	2.4
16.5	0.7	0.7	71	1.3	0.8	83	1.0	0.8

Table 6.1: Table showing the calculated e-folding time scales for station 1-3. z is the depth in meters. τ_N is the time scale for the flow normal to the isobaths and τ_P is the time scale for the flow parallel to the isobaths.

6.2.

Station 1			Station 2			Station 3		
z	τ_N	τ_P	z	τ_N	τ_P	z	τ_N	τ_P
9	1.6	1.2	8	3.3	0.9	16	0.7	0.9
15	0.7	0.7	11	1.0	1.0	36	0.7	0.9
24	2.1	0.9	14	0.8	0.8	56	1.2	0.6
33	1.1	0.8	23	3.0	0.9	76	0.9	0.7
42	3.4	1.9	32	1.0	0.9	96	1.0	0.7
51	0.9	0.7	41	0.6	0.7	116	0.7	0.9
60	1.8	1.5	50	0.7	0.9	136	1.1	0.8

Table 6.2: Table showing the calculated e-folding time scales for station 4-6. z is the depth in meters. τ_N is the time scale for the flow normal to the isobaths and τ_P is the time scale for the flow parallel to the isobaths.

For the flow along the isobaths, surface e-folding time scales of around 1.2 days are often found near Bastøy (see Table **??**). The typical bottom value for the same area is usually around 0.7 days. At station 1, the time scale decreases steadily towards the bottom, whereas at the other stations it fluctuates more. For instance, values up to 2.9 days are found near the bottom at station 3. In the Drøbak Strait, the time scales are generally smaller for the isobath-following component, typically less than unity.

Across the isobaths, the currents seem to be slightly more persistent. In this component, time scales of up to 4.0 days are observed. Near Bastøy, the time scales are typically between 0.6 and 1.7 days, with some larger values at a few intermediate depths. At the Drøbak Strait, the time scales are often around 0.7-0.8 days, but there are some depths with values of 2-3 days too. In general, these time scales agree quite well with the fact that the peaks in the Hovmöller diagrams (Section 6.2) typically last for 1-3 days.

We can see that the autocorrelation function in Figure 6.8 looks like a cosine times exponential function rather than a pure exponential function. Therefore, another possible estimate of the autocorrelation function is $r(t_j) \propto e^{-t_j/T_1} \cos(t_j/T_2)$. In this formula there are two time scales, of which T_1 resembles the e-folding scale while T_2 is a time scale representing the fluctuations. T_1 is often found to be less than the integral time scales obtained in the previous paragraphs.

A third method to determine integral time scales is also used. The method comprises taking the asymptotic value of the cumulative sum of the autocorrelation and multiply it by dt (see Section 5.3). This often gives values close to zero (see e.g. Figure 6.9). Therefore, the average value where the cumulative sum is approximately constant is used instead. Because the graphs fluctuate much, it is hard to find this constant value. Nevertheless, values in the range 0.7-1 day are often found. There are also a few depths with larger

values, up to 4-5 days (mostly across the contours).

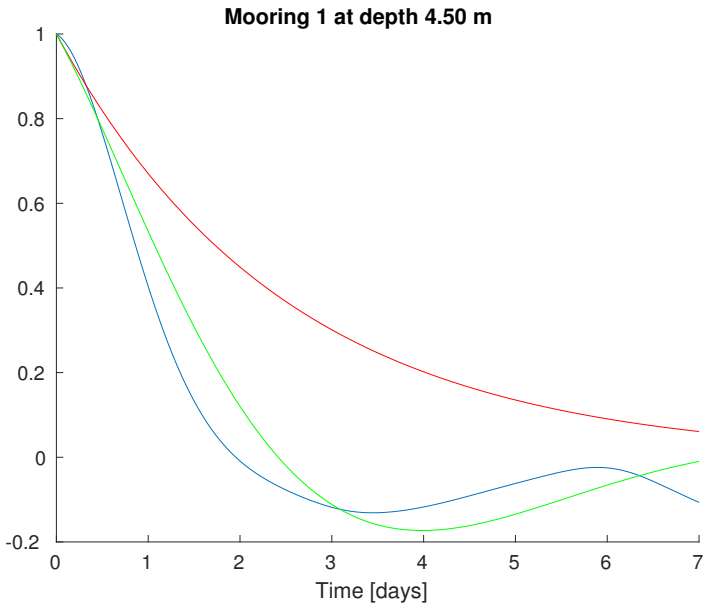

Figure 6.8: Example plot of autocorrelation function (blue curve) together with exponential function (red curve) and exponential times cosine function (green curve). Station 1 at 4.5 m depth.

Neither the harmonic analysis nor the Butterworth filter are perfect techniques for removing the tides. It is still a little bit surprising to find time scales that are less than a day for the filtered currents. In Section 5.3, we see that the integral time scale is proportional to the inverse of the peak frequency in the PSDs. If we use this fact, we can deduce the time scales from the de-tided PSDs. This gives the longest time scales at the stations south of Bastøy, which are closest to the open ocean. These stations get time scales of about 4 days, while the stations in the Drøbak Strait get time scales of about 2 days (although for some depths around 5 days).

As mentioned in Section 5.3, the time scale must be well resolved by the averaging period. The shortest time scale is about 0.6 days. The maximum averaging period of 4 minutes is about 0.5% of this time scale. Thus, the time scale is fairly well resolved. However, considering that it is in fact 10 minutes between each recording, the percentage increases to 1-2%.

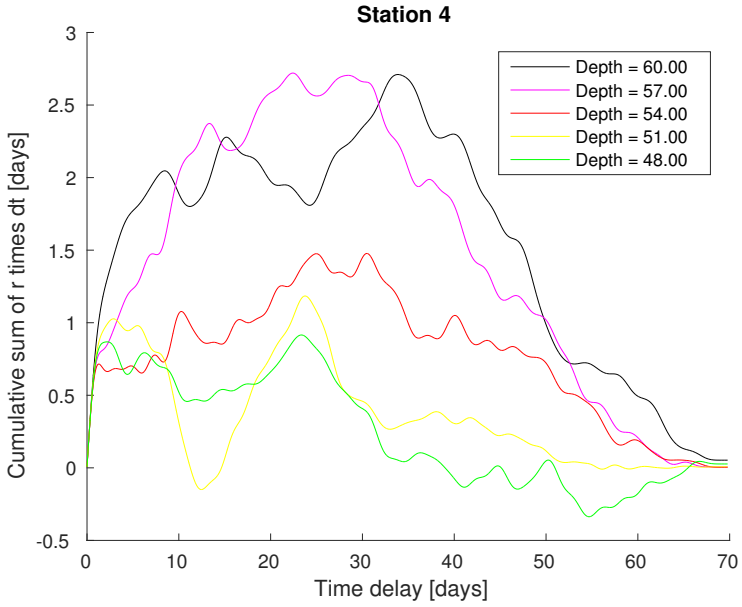

Figure 6.9: Example plots of the convergence values for the autocorrelation functions. Station 4 near the bottom, flow normal to the contours.

6.4 Variance ellipses

Variance ellipses give information about both the variance and the current direction. Firstly, they show where the variance is greatest. The wider the ellipse, the more variance in the data. Furthermore, they show directional patterns, for instance how the current turns with depth. If plotted in a map (like here), they can also show how the current direction compares to topography. Horizontal variations in flow direction can also be detected.

Figure 6.10, 6.11, 6.12, 6.13, 6.14 and 6.15 shows examples of variance ellipses for the low-passed velocities at each station. The variance is greatest at station 1 and 2, where the current is strongest (see Section 6.2). Values up to 0.2 ms^{-1} occur along the major axis. Station 3, 5 and 6 have 0.1 ms^{-1} variance along the major axis near the surface. Station 4 clearly has the least variance. Along the minor axis, the variance is typically in the range 0.01-0.1 ms^{-1} for all the stations.

The variance is always greatest near the surface. It typically decreases smoothly with depth, except at station 3. At this station, there is a small oceanic shelf in the vicinity. Near the bottom, the variance goes down to about 0.01-0.05 ms^{-1}. The largest bottom values are found near Drøbak (station 5 and 6), where the fjord is narrowest. Previously, we have seen that the parallel flow dominates at these stations (Section 6.2).

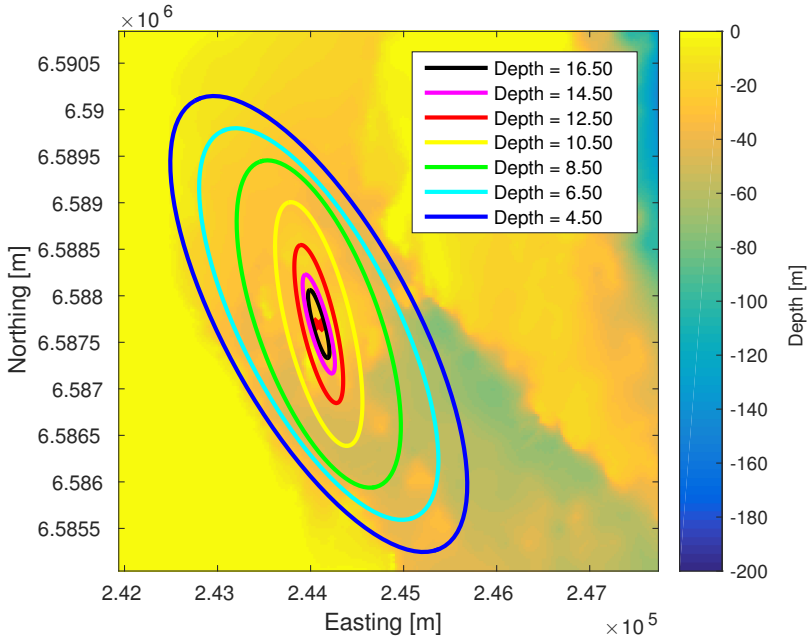

Figure 6.10: Variance ellipses at station 1.

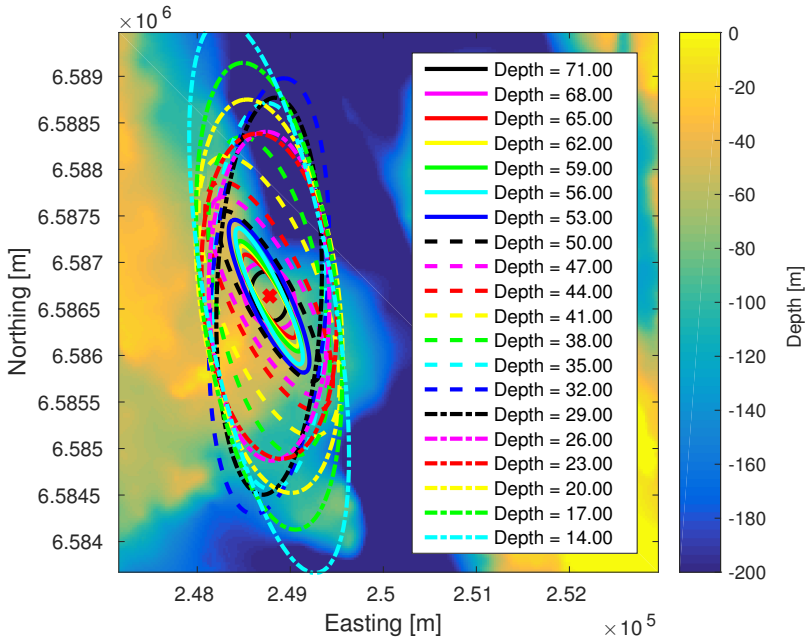

Figure 6.11: Variance ellipses at station 2.

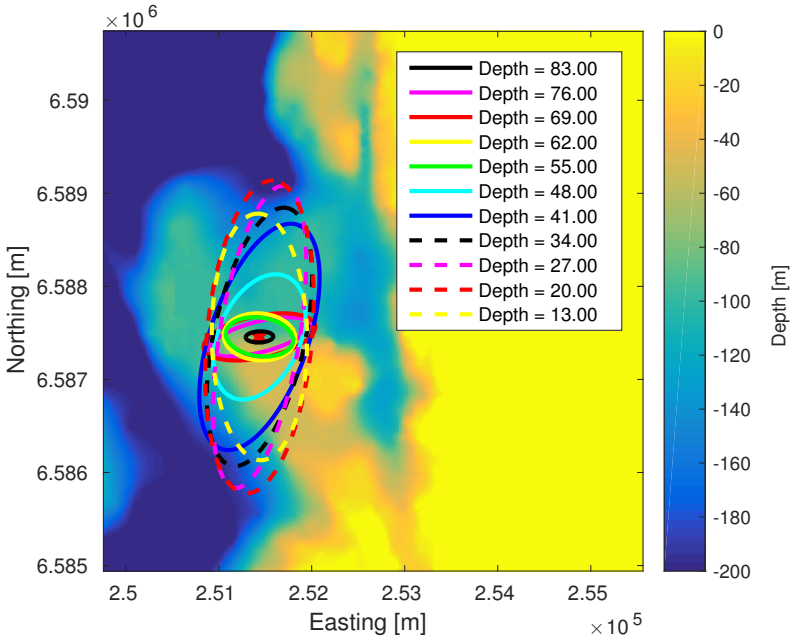

Figure 6.12: Variance ellipses at station 3.

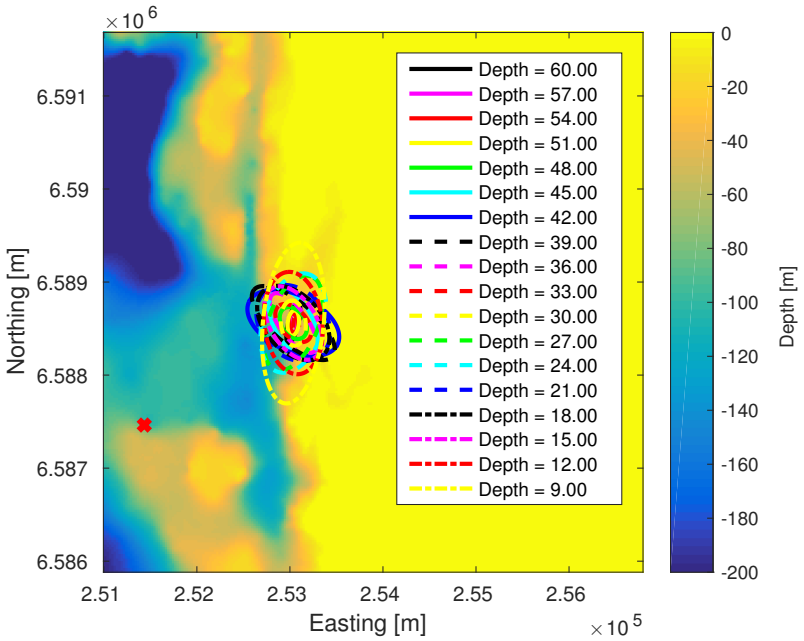

Figure 6.13: Variance ellipses at station 4.

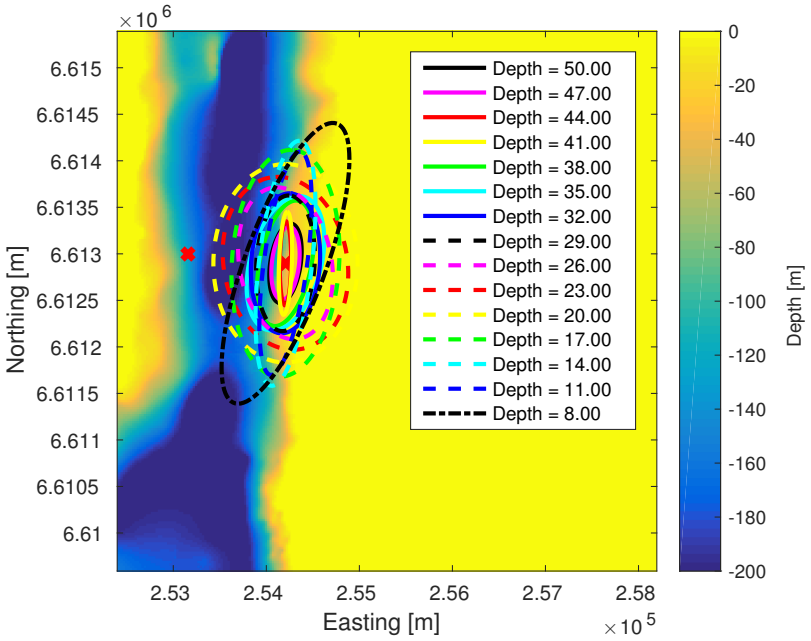

Figure 6.14: Variance ellipses at station 5.

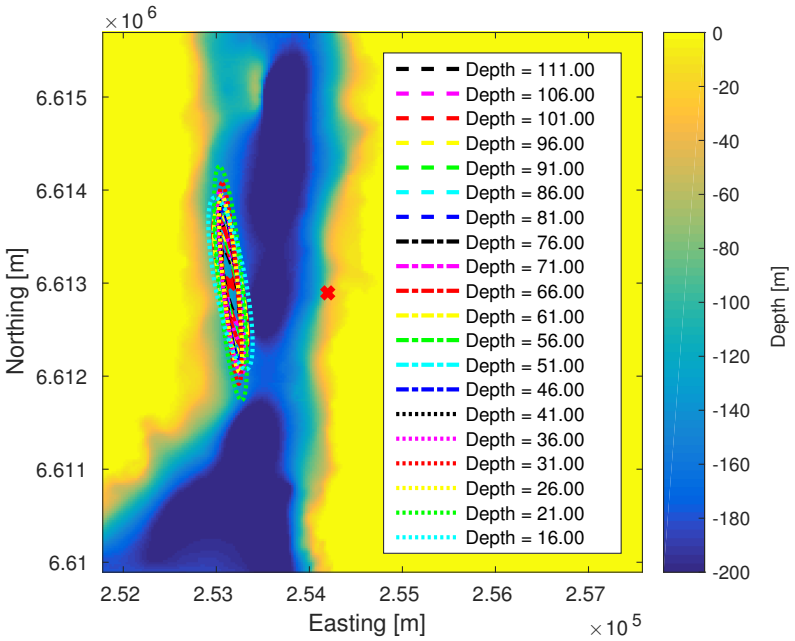

Figure 6.15: Variance ellipses at station 6.

From the Figures, we can see that the ellipses often turn clockwise with depth near the surface. For some of the stations, the turning direction switches between being clockwise and anticlockwise many times. At the shallow station 1 and at station 6, on the other hand, a more or less constant flow direction is found. The variance ellipses near the bottom are usually oriented along the isobaths. At station 4, however, they are aligned with the slope instead. As mentioned earlier, this station is sheltered from the mean flow. Most of the ellipses are more or less oriented along-fjord. The fjord is of comparable width to a Rossby radius, implying that effects of the Earth's rotation is of minor importance. The only places where the flow is perpendicular to the fjord shape is at station 3 near the bottom and at station 4 at mid-depth.

One can get extra insight into the current directions by considering the mean flows. From these, it is found that the flow goes northwards on the east side of the Drøbak Strait and southwards on its west side. This is a typical circulation pattern in fjords where the Coriolis force is important. On the east side of Bastøy (station 2), the flow is mainly due north, while on its west side it is due south. Otherwise, the direction is quite variable.

6.5 Probability density functions

All the statistical moments derive from the PDF. Thus, one is able to see for instance the skewness in the data. Are the currents mostly close to the mean, or do they deviate significantly from the mean? In other words, the structure of the PDF has implications for the temporal variation of current.

The Kolmogorov-Smirnov test gives a value of 1 for all the measurements. This means that the PDFs are statistically Gaussian, i.e. normally distributed. Thus, no deviations in the data are significant from a statistical point of view. However, the record length is relatively short, i.e., less than a year. With a longer measurement duration, the deviations could have been more significant.

Figure 6.16 shows an example of a PDF, together with a Gaussian curve. We can see that the distribution looks somewhat skewed. This is the case for most of the PDFs at station 1 and 2. These stations are closest to the largely freshwater affected Drammensfjord. At these stations, the most frequently occuring current has a more negative component along the isobaths and a more positive component across the isobaths, compared to the mean.

In accordance with the above results, the skewness for station 2 is positive (vertical mean 0.19) across the isobaths and negative (vertical mean -0.48) along the isobaths. At station 1, however, the skewness is negative (vertical

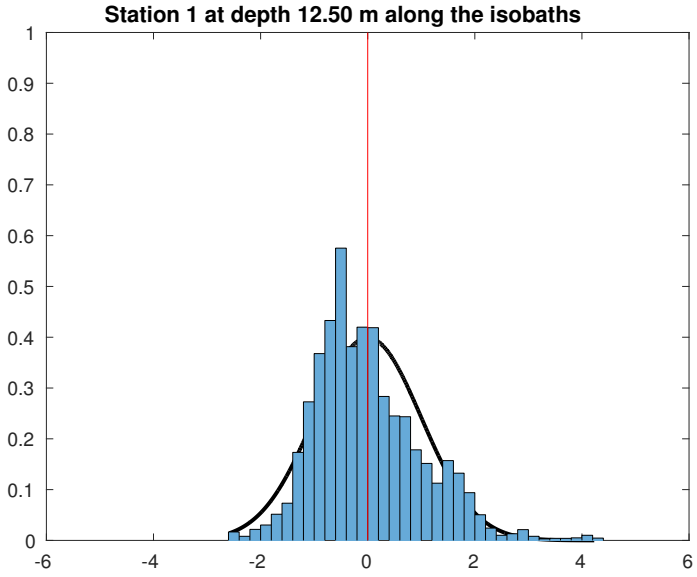

Figure 6.16: PDF plot for station 1 along the isobaths at 12.5 m depth.

mean -0.77) across the isobaths and positive (vertical mean 0.75) along the isobaths. This is because of peaks in the far left (left tail) along the isobaths and in the far right (right tail) across the isobaths (mostly near the surface). The other stations also have significant tails at specific depths. Station 3 has a negative tail near the surface along the topography. At about 50 m depth, negative tails are found along the isobaths at station 4. Moreover, at station 5 there are positive tails in the across component near the surface.

6.6 Empirical orthogonal functions

In this thesis, the main purpose with empirical orthogonal functions is to find typical vertical variations in the flow. The structure of the EOFs could for instance resemble barotropic or baroclinic modes with different kinds of stratification. It might also differ significantly, for instance if there are large values at intermediate depths or near the bottom. Furthermore, one can find out how much percentage of variance that is covered in a specific EOF. Is for instance the first EOF very dominant?

In Figure 6.17 and 6.18, we can see the EOFs covering the largest amount of variance at each station. From these plots, we can see that the most dominant EOF often has a strong gradient near the surface. Some EOFs, however, peak near mid-depth instead. We have previously seen both surface

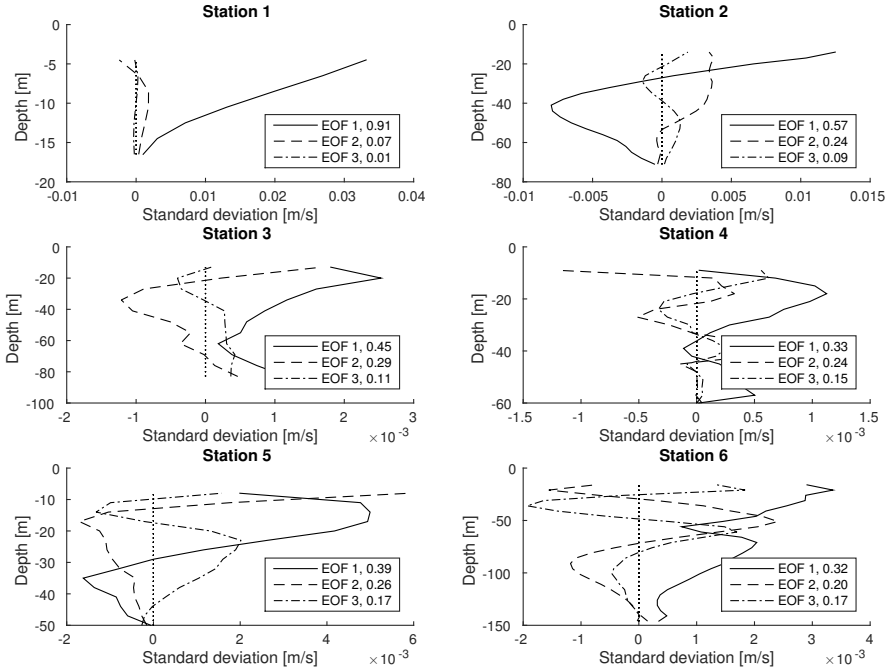

Figure 6.17: EOFs for the flow parallel to the contours. The decimal numbers are the fractions of total variance covered by each EOF.

and intermediate current events in the Hovmöller diagrams presented earlier (see Section 6.2).

Most of the EOFs go to zero near the bottom. At station 3 and at station 4 along the contours, on the other hand, the amplitude increases near the bottom. This might be an effect of topographic waves as well. In the Hovmöller diagrams, we saw that station 2 and station 4 had intensified flow near the bottom. This occurred mainly in the normal component.

Usually, there is more variance in the EOFs along the contours. This is seen at station 1, 4 and 6. We have seen that the current often is following the isobaths. At station 3 and 5, the amount of variance is approximately equal for both components. The cross-isobath EOFs have most variance at station 2, however. We have already seen that this station has strongest flow across the isobaths.

The primary EOFs for station 1 and 6 do not change sign with depth. From Section 6.4, we recall that these were the stations with the least changes in direction. Station 3's most important EOF also has the same sign throughout, but in contrary to the aforementioned stations, which have a fairly

smooth shape, it has a zigzag shape. The best examples of zigzags, however, are the EOFs at station 4 and 5 (normal to the contours). At these stations, we have seen that the direction changes much with depth (see again Section 6.4).

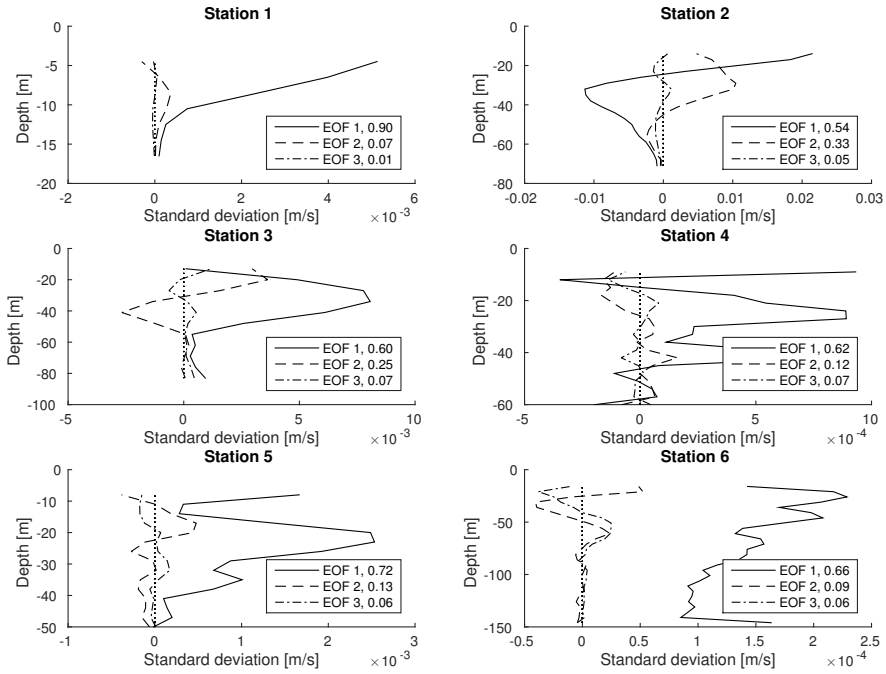

Figure 6.18: EOFs for the flow normal to the contours. The decimal numbers are the fractions of total variance covered by each EOF.

The variance covered by each EOF is also shown in Figure 6.17 and 6.18. We can see that at station 1, about 90% of the variance is in the primary EOF. Normally, only 40-50% of the variance is in the first EOF. This percentage is larger for the normal component of the flow, which tends to be the weakest component.

We can see that the EOFs have some resemblance to baroclinic modes with rough bottom, see Figure 2.1. The first mode is found at station 1. Similarities to the second mode can be observed at station 1 and 2, as well as at station 3 and 5 along the contours. Higher baroclinic rough bottom modes can also be found. The presence of these modes shows that the flow is significantly affected by bottom roughness. It also shows that there is some stratification at these locations, possibly near-exponential (see Section 2.2).

6.7 Model validation

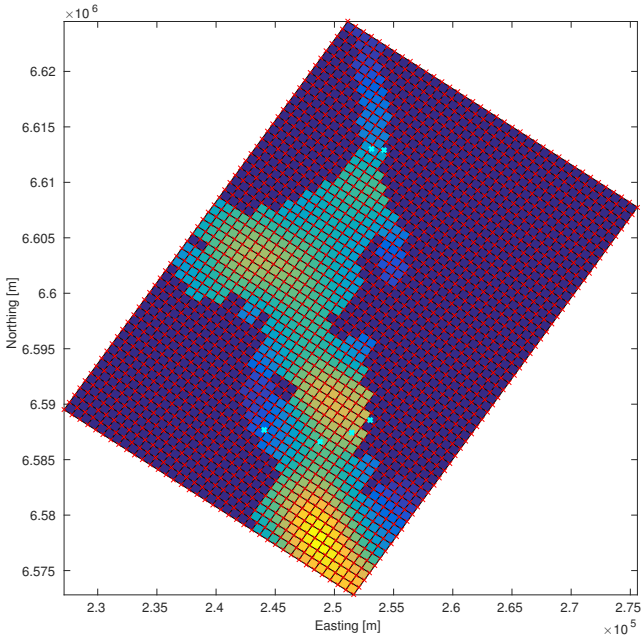

Figure 6.19: Plot of the model grid. Red crosses indicate grid points and cyan crosses are the real station locations.

In this chapter, the model output is presented and compared to the measurements. Figure 6.19 shows a portion of the model grid that covers the locations of the six moorings. Notice that the model grid is too shallow. For instance, the deepest trenches are less than 200 m deep while in reality being close to 300 m deep. At station 6, the model is about 50 m while measurements stretch down to 150 m. This is due to the smoothing of the grid, which is done to avoid numerical noise.

In the comparison, the closest grid point to each station is chosen. Hovmöller diagrams, variance ellipses and empirical orthogonal functions are plotted. As mentioned earlier, the output files used here have a temporal resolution of 1 day. Thus, the autocorrelation functions only give a rough estimate of the e-folding time scale, which is found to be about 1-3 days. The measurements gave values in approximately the same range. The frequency spectra for the model were found to be of minor importance, due to the lack of tidal periods. PDFs were also omitted because there is not enough data.

6.7.1 Hovmöller diagrams

Figure 6.20, 6.21, 6.22, 6.23, 6.24 and 6.25 shows the Hovmöller diagrams for the grid points closest to each station. We can see that the strongest currents are found near station 3 and 6. There are also fairly energetic currents near station 5. In the measurements, the largest values were found near Bastøy, i.e. at station 1 and 2. Recall that the local bathymetry is slightly different.

The model current strengths are up to 0.6 ms^{-1}. On average, the model output gives currents of about 0.3-0.4 ms^{-1}. The observations have maximum values of about 0.4-0.5 ms^{-1} and average values between 0.1 and 0.2 ms^{-1}. In general, the model grid is shallower than the real bathymetry of the Oslofjord.

The flow is typically about equally strong along and across the contours. Near station 2 and 5, the current is slightly stronger along the isobaths, while near station 3 the opposite is seen. Close to station 6, the flow across the contours is clearly strongest. It is up to 0.5 ms^{-1}, while it never exceeds 0.3 ms^{-1} along the contours. This is exactly the opposite of what we saw in the measurements.

In the measurements, it is possible to distinguish between different layers of current. This is not as easy in the model output, which has a low vertical resolution. Nevertheless, there seems to be a surface layer. The surface events have a typical vertical extent of about 5-12 m. They sometimes stretch deeper down, however, almost reaching the sea floor. The typical surface peak duration is around 2-3 days. Station 5 has a few current maxima which last for about a week. 1-3 days is a more common value for the measurements, which have a finer temporal scale (10 minutes). The model peaks occur about 4-6 times per month. The corresponding number for the measurements is about 2-4 times per month.

Occasionally, it is possible to see weak signs of return flows at intermediate depths. These flows are never stronger than the surface flows. In the data, we see that there are situations were the intermediate flow is the strongest flow. There is a lack of measurements from the uppermost few meters, though. The peaks have typical vertical extents of 5-20 m. This is approximately in the same range as for the measurements.

In Section 6.2, we see that the flow usually decays near the bottom. We also see that it gets particularly weak across the contours. Furthermore, we see that there are some cases where it is strong near the bottom. All of these features can be seen in the model too. Thus, topographic waves might be resolved in the model.

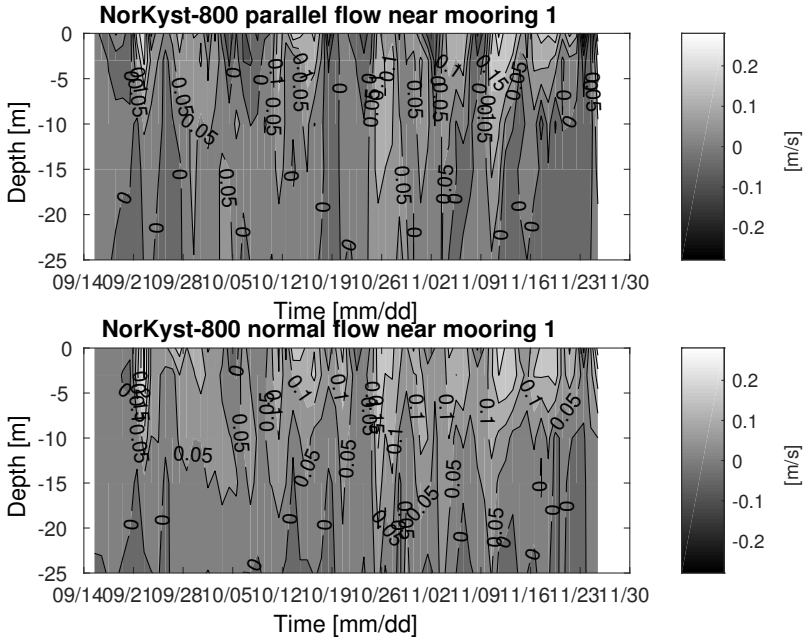

Figure 6.20: Hovmöller diagram for parallel and normal flow near station 1.

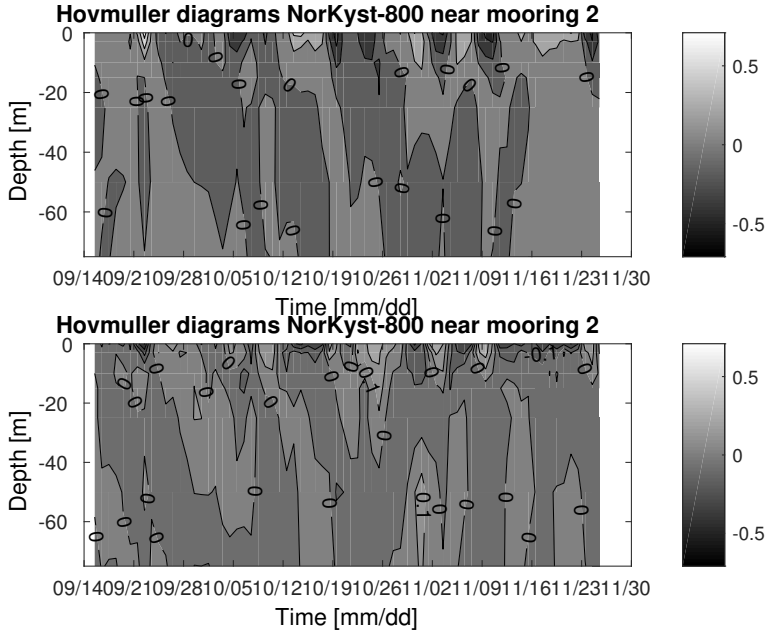

Figure 6.21: Hovmöller diagram for parallel and normal flow near station 2.

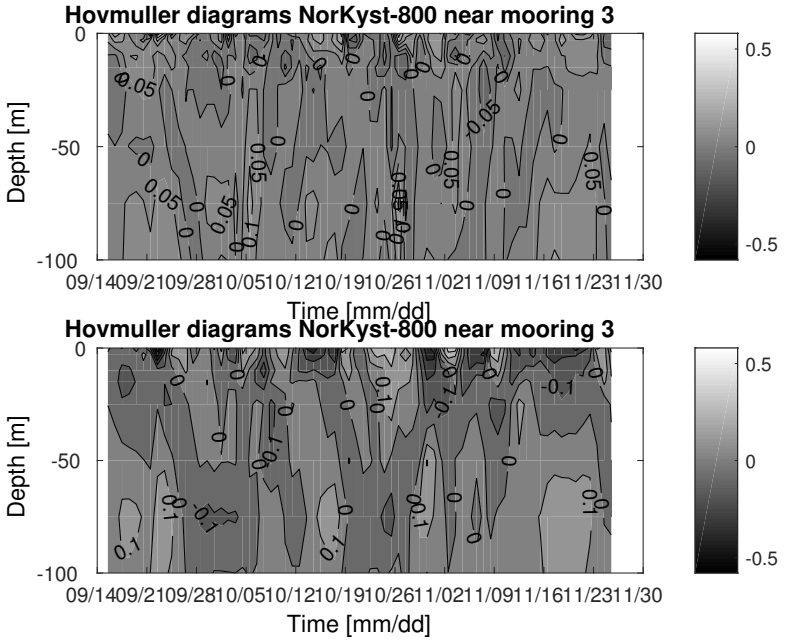

Figure 6.22: Hovmöller diagram for parallel and normal flow near station 3.

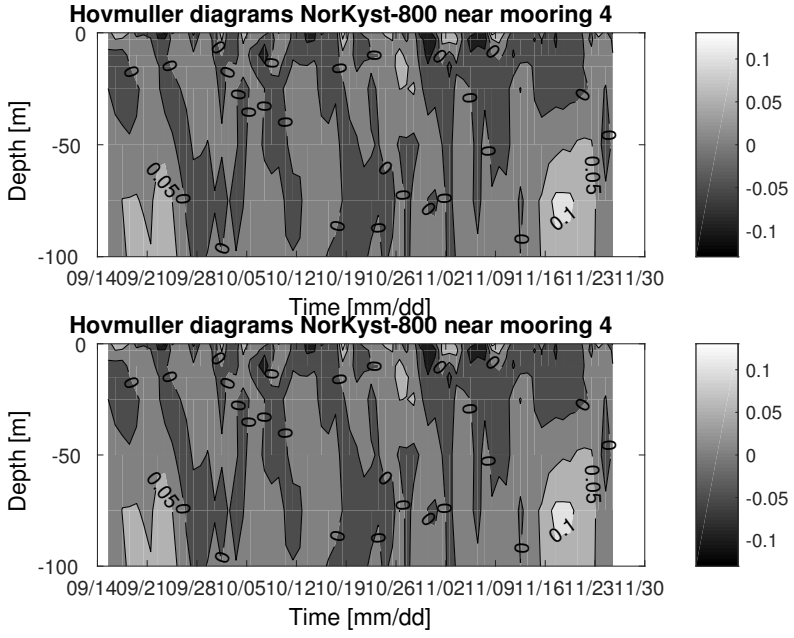

Figure 6.23: Hovmöller diagram for parallel and normal flow near station 4.

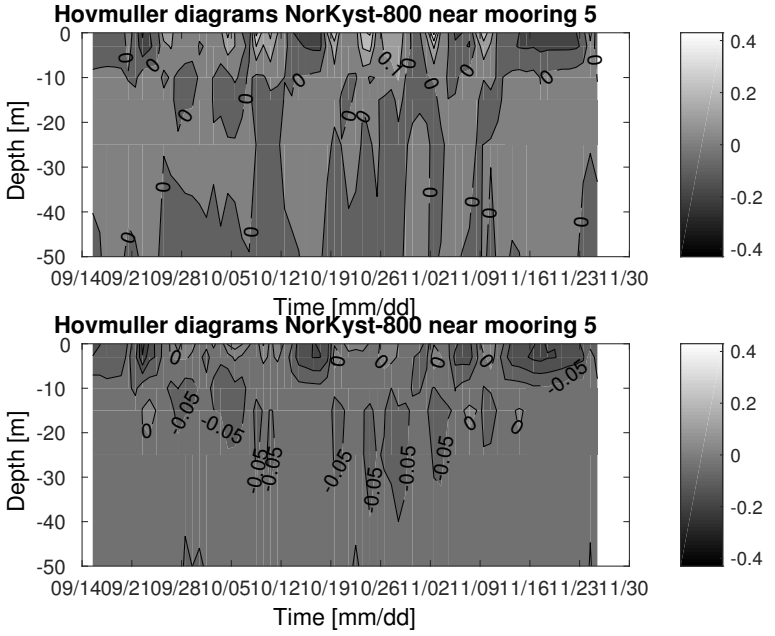

Figure 6.24: Hovmöller diagram for parallel and normal flow near station 5.

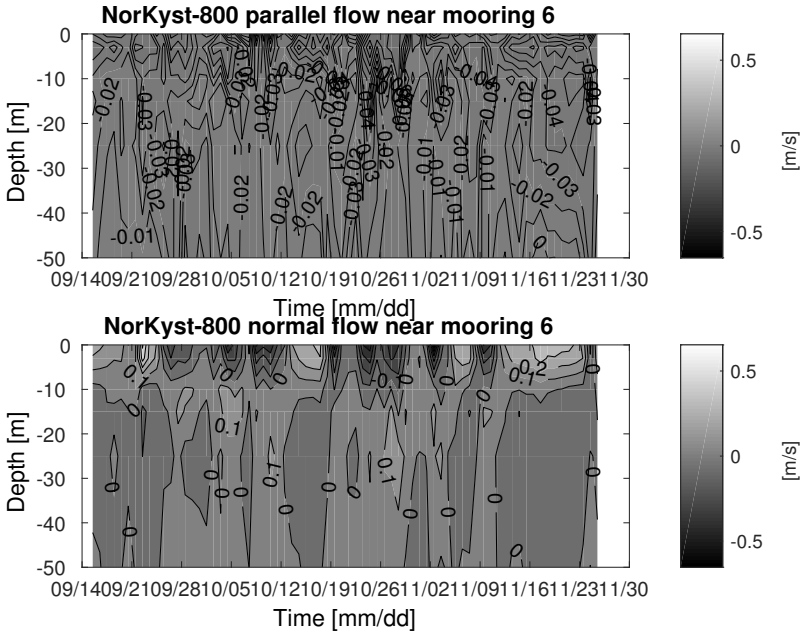

Figure 6.25: Hovmöller diagram for parallel and normal flow near station 6.

6.7.2 Variance ellipses

In Figure 6.26, 6.27, 6.28, 6.29, 6.30 and 6.31 variance ellipses for model grid points are plotted. The variance is strongest near station 1, with values up to 0.4 ms^{-1}. In the data, the maximum variance is 0.2 ms^{-1}. The current strengths are fairly weak at this station. Station 3 and 6, which have the strongest currents, also have a fairly large variance. The smallest values are found at station 4. This is also observed in the measurements. The variance decreases quite smoothly with depth, and near the bottom the variance decreases to about 0.01-0.03 ms^{-1}. The largest bottom values are found near station 2 and 3. Slightly larger bottom variance is found in the measurements.

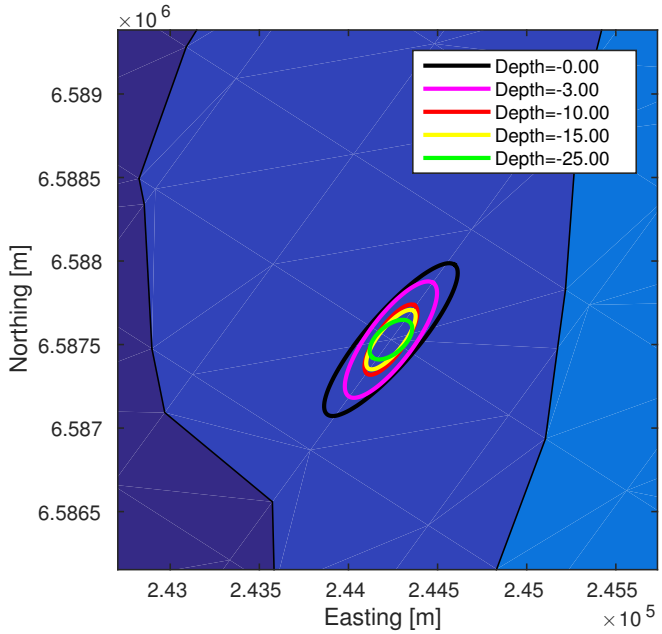

Figure 6.26: Variance ellipse from the model near station 1.

The ellipses often turn anticlockwise with depth near the surface. Further down, they turn clockwise. In the meantime, a predominantly clockwise turning with depth is found to dominate in the measurements. Most of the model ellipses are oriented to the northeast. We recall that the ellipses in the data tend to align with the fjord. Near the bottom, the model ellipses are usually aligned with the bathymetric contours. This also applies to the data.

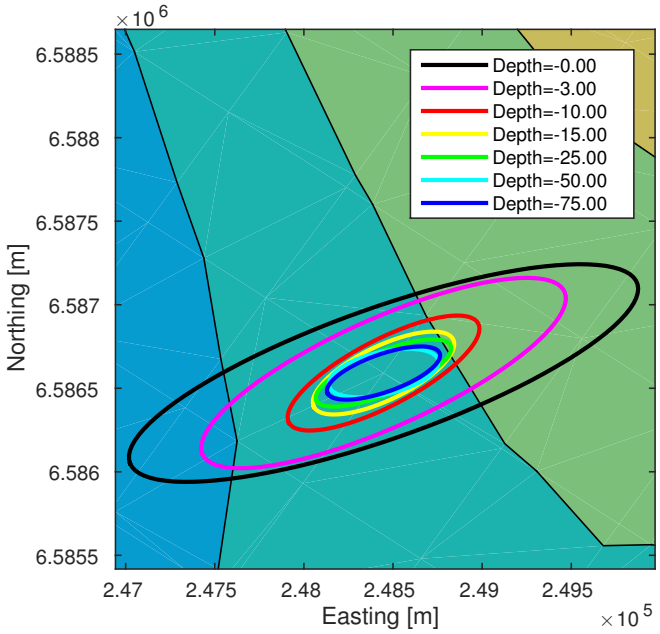

Figure 6.27: Variance ellipse from the model near station 2.

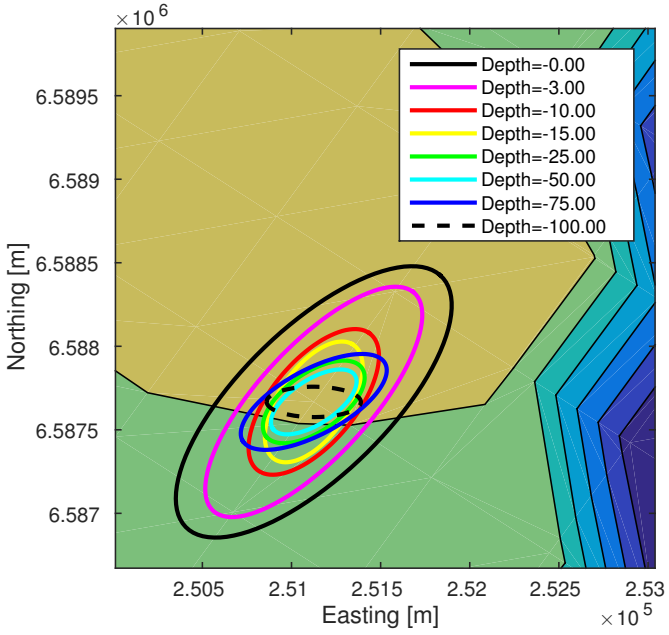

Figure 6.28: Variance ellipse from the model near station 3.

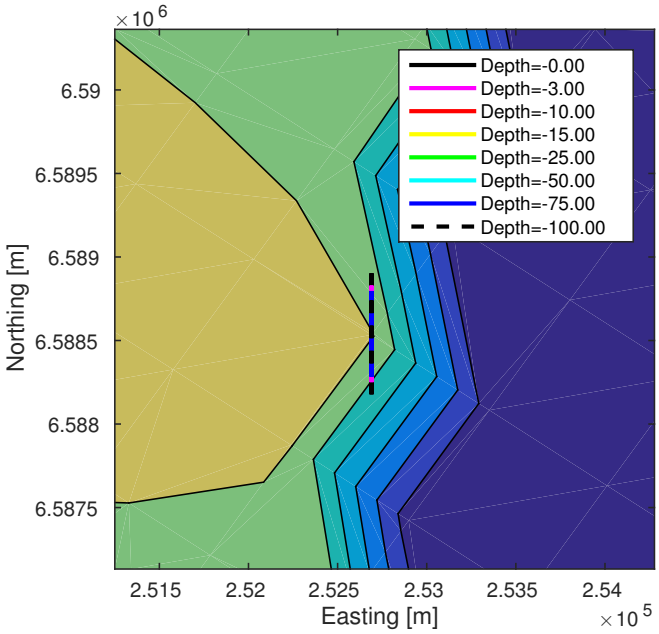

Figure 6.29: Variance ellipse from the model near station 4.

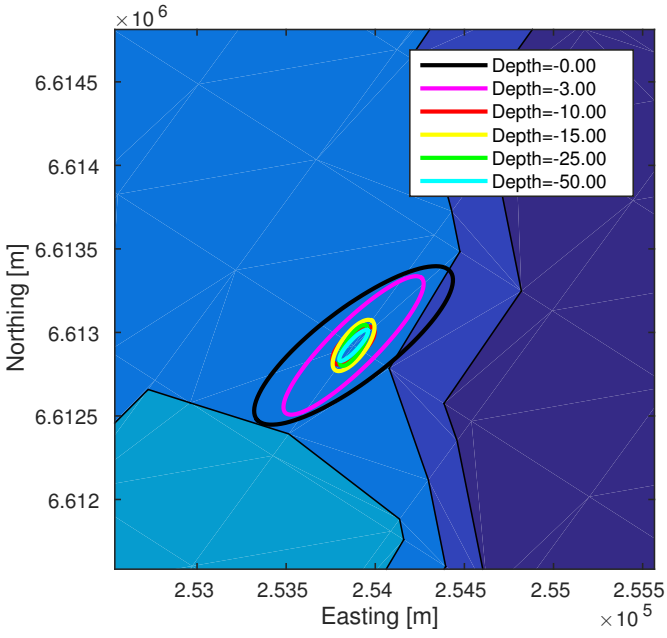

Figure 6.30: Variance ellipse from the model near station 5.

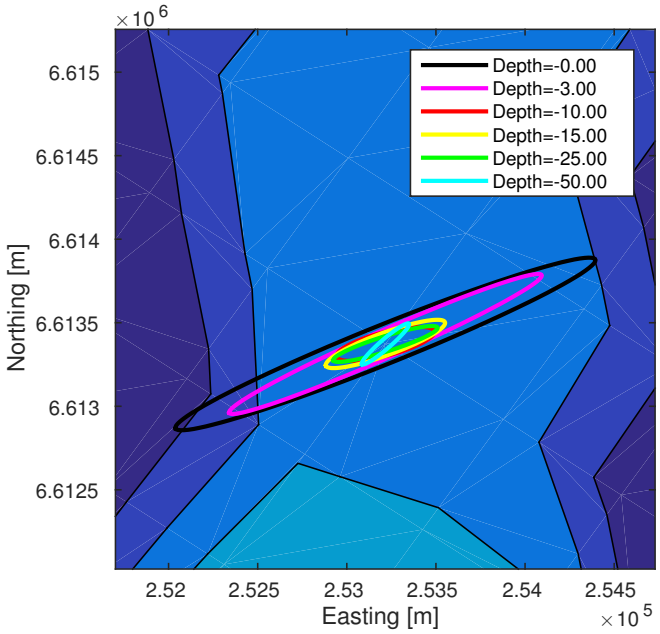

Figure 6.31: Variance ellipse from the model near station 6.

6.7.3 Empirical orthogonal functions

In Figure 6.32 and 6.33, EOFs from the model have been plotted along and across the topography, respectively. There is a strong gradient near the surface, especially in the first EOF. We see this surface gradient in the measurements (Section 6.6), as well as in the model Hovmöller diagrams. No mid-depth maxima are present. However, the model vertical resolution is not as good as for the measurements. A decay of variance is observed in the model output near the bottom. In the data, variance increase is seen towards the bottom at some stations (in particular station 3 and 4). This relatively small scale feature can not be found in the model output. The model vertical resolution gets worse with depth, however.

The magnitude of the variance is fairly similar for the two components. There is an exception to this near station 6, where the component normal to the isobaths dominates. Previously, we have seen that the modeled current at this station is strongest across the isobaths as well.

We can see that for many of the chosen locations, the primary EOF has a very simple structure. Most of the time, it does not cross the zero line. Furthermore, there is typically a smooth increase in amplitude towards the surface. For some of the grid cells, this EOF changes sign once or twice. In Section 6.6, we see that the leading EOF for the data has a quite complex

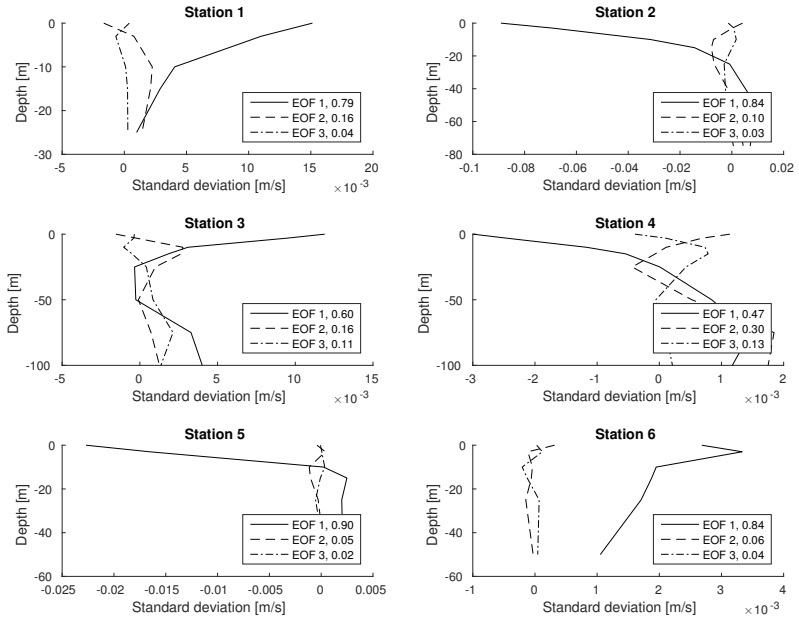

Figure 6.32: EOFs for the parallel flow near each station.

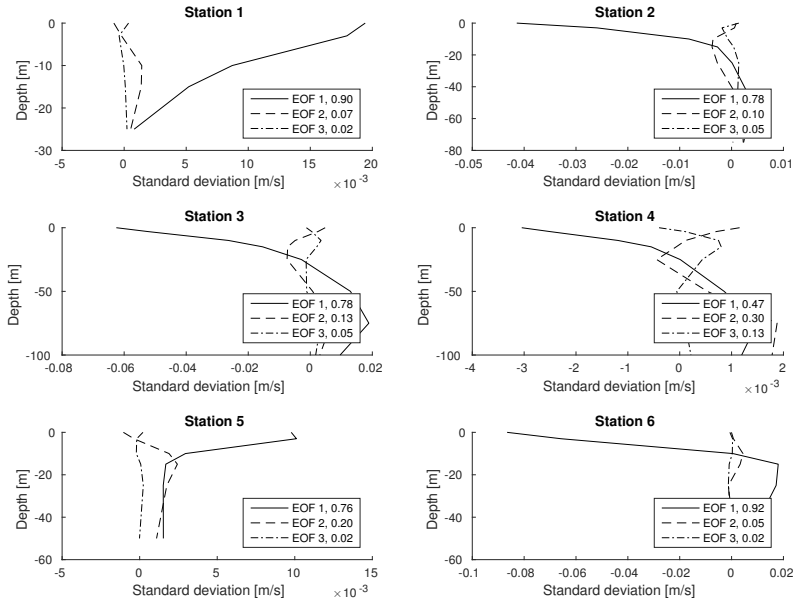

Figure 6.33: EOFs for the normal flow near each station.

structure some places.

We can see that the primary EOF often covers more than 70% of the variance. The percentage is up to 90% some places. In the measurements, we see that the first EOF normally only accounts for about 40-50%. There is not a big difference in variance between the parallel and normal flow components. The only exception is found near station 6, where the normal component dominates. The measurements give a different picture, always having dominating components normal to the contours.

In the measurements we can observe baroclinic modes with rough bottom. Resemblances of the first baroclinic mode is present in the model output as well. An example of this is the most significant EOF at station 1. Similarities to the second baroclinic mode is occasionally important as well. It is rarely a dominating trend though.

Chapter 7

Summary and conclusions

In this study in-situ measurements from the Outer Oslofjord are analyzed with different statistical tools. Hourly output from similar locations in the NorKyst-800 model grid are analyzed in a similar manner. PSDs are calculated for the raw data. Two ways of de-tiding the raw data are applied; harmonic analysis and Butterworth filtering. The filtered currents (and the model output) are plotted in Hovmöller diagrams. Autocorrelation functions are found, in addition to variance ellipses, PDFs (only for the data) and empirical orthogonal functions.

When it comes to tides, the M_2 frequency dominates. Harmonic overtides of the M_2 component are also seen. This finding agrees well with Staalstrøm et al. (2012) and Stigebrandt (1979). Staalstrøm et al. (2012) argues that internal tidal waves propagate in the Drøbak Strait. The measurements substantiate this statement, because the peak of the M_2 frequency at station 5 and 6 is at about sill depth (20 m). Near Bastøy, the M_2 component has a deeper peak, possibly due to the strong stratification gradient there. Close to the coast (station 4), other tidal frequencies are found to be more important. Usually, the non-tidal frequencies are the most important ones. Some of them are unphysical, probably due to the shortness of the time series.

The Hovmöller diagrams show that the strongest currents are near Bastøy, with maximum flow speeds of 50 cms^{-1}. This is possibly due to the freshwater flux from Drammenselva or very shallow measurements (station 1). The weakest flow is found at station 4. The flow tends to follow the isobaths, except at station 2, where the isobaths are at right angles with the coastline. One can distinguish between two layers of current. The fluctuations in the surface layer are most likely driven by winds, although the freshwater input could also affect it. This is in accordance with Staalstrøm et al. (2012). In the second layer, the flow often reverses, which might be a sign of an estuarine circulation. The currents are sometimes strongest in this layer, perhaps due

to missing records near the surface. Near the bottom, the flow is normally weak, feeling the friction from the seafloor. However, it intensifies some places as well. Topographic waves with wavelengths of about 3 km might be the reason for this. This is particularly likely to happen at station 3 and station 4 because the isobaths at these locations are perpendicular to the general flow direction.

Various ways of interpreting the autocorrelation functions gave integral time scales of about a day. Slightly longer time scales were found near the surface. Occasionally, large values were found at some intermediate depths, up to 3 days. These observations do not agree with the model study done by NIVA (Section 1.1), which finds time scales of 4-6 days in the Oslofjord. However, short time scales are observed other places, for instance at the shelf off the west coast of Norway (LaCasce, 2005b). Here, time scales of 1-3 days are found for the low-passed current, with larger values near the surface (in the Norwegian Atlantic Current core). Furthermore, Roberts and Roberts (1978) obtains time scales of 2-3 days in the Gulf of Alaska (with a cutoff frequency of $1/3h^{-1}$). Deduction from the peak frequency of the PSDs gives longer time scales. Near Bastøy, the time scale is then about 4 days, while typically being 2 days in the southern Drøbak Strait.

The variance is greatest where the strongest currents are found. The ellipses follow the isobaths near the bottom. This could be connected with the topographic waves mentioned earlier, which propagate along the isobaths. There is a weak clockwise turning of current with depth near the surface. This resembles the results of other studies elsewhere, like Kundu (1976) and Lenn and Chereskin (2009). These argued that it could be signs of Ekman currents (Ekman, 1905). Broadly speaking, the variance tends to align with the fjord shape, in particular in narrow areas like the Drøbak Strait. This agrees well with Johannessen (1967), which found currents following the fjord shape in the inner fjord. The mean current vectors show that the circulation resembles that of fjords which are significantly affected by the Coriolis force, even though the Rossby radius is not well resolved by the fjord width.

There is some deviation from the normal distribution at the stations closest to the Drammensfjord. It might be that the freshwater flux is what causes these deviations, although they are not only found in the surface. They could also be related to the closeness to Bastøy. The Kolmogorov-Smirnov test, however, shows that the currents are statistically Gaussian. LaCasce (2005b) found non-Gaussianity in the flow offshore of the western Norwegian shelf. However, the record was longer and in the middle of a strong, already known current. Bracco et al. (2000) found PDF plots with extended wings in the Northern and equatorial Atlantic Ocean and explained these with the existence of eddies.

From the EOFs, one can recognize several features that could also be seen in the Hovmöller diagrams. This includes flow intensification near the surface and flow weakening near the bottom. Occasionally, the EOF has an increasing amplitude near the bottom along the isobaths, which fits well with the existence of topographic waves. The primary EOF is almost constant at station 1 and 6, in consistence with the little degree of turning at these stations. At station 4 and 5, which have much direction change with depth, the EOFs have zigzag patterns. About 40-50% of the variance is normally covered in the primary EOF. The percentage tends to be largest in the normal component, possibly because it has weaker flow. 90% variance is covered in both components at station 1, due to its simple flow structure. Baroclinic rough bottom modes are found. Hall (1986) found the first baroclinic mode to be important along the Gulf Stream. Here, winds or freshwater pulses could excite the 1st baroclinic mode. The 2nd baroclinic mode could be associated with the return flow in the estuarine circulation. Gade (1968) found both estuarine circulation and wind driven circulation to be important in the Oslofjord.

The model has strongest currents at other locations than the measurements. This could be due to differences between the model grid and the real bathymetry, for instance. Furthermore, it slightly overestimates the currents in general, probably due to that the grid is too shallow, requiring higher velocities for equal volume flux. The two flow components have a similar magnitude, except near station 6 where the normal flow component is clearly strongest. The reason for this might be that the model bathymetry is fairly smooth, so that it can not affect the dynamics as much as it does in reality. A surface layer is seen in the model output, but the peaks last longer, probably due to a lower temporal resolution. There is also a weak intermediate layer a few places. Near the bottom, the flow intensifies sometimes, possibly due to topographic waves like in the data.

Analogously to the stronger currents, the model also has more variance in general. It decreases more smoothly than in the measurements. Instead of turning clockwise, the model output gives ellipses that turn anticlockwise with depth near the surface. The most typical orientation direction is north-eastwards/ south-westwards.

A strong gradient is found in the model's primary EOFs near the surface. There is little evidence for mid-depth maxima, just like in the model Hovmöller diagrams. A difference to these Hovmöller diagrams, however, is that the EOFs do not capture bottom intensification. The first EOF in the model captures more variance than in the measurements. Baroclinic modes with rough bottom can be seen in the model output.

Possible future improvements for this thesis include increasing the record-

ing period, for instance to one year. This would increase the reliability of the statistics used. In particular, it would make it more likely to find statistically significant deviations in the flow. In addition, it could reduce the uncertainty in the autocorrelation functions. Error estimates for the results, such as the e-folding time scales, could be useful as well.

The number of instruments could be increased so that it is easier to see horizontal changes, for instance in the variance ellipses. In LaCasce (2005b), several tens of instruments were used, and horizontal patterns were thus easier to detect. However, this study was done in an area where the bathymetry was of major importance. Another advantage could be enabling calculation of force magnitudes in the Navier-Stokes equation. This requires a fairly high spatial resolution because of horizontal gradients. In addition, spatial coherence scales would be easier to estimate, see e.g. (LaCasce, 2005b).

Analyzing Hovmöller diagrams, variance ellipses and empirical orthogonal functions for the tidal currents could also be an useful advancement. This could give more insight into the role of the tides in the fjord. For instance, the ellipses could show how the tides affect the directional patterns of flow. Moreover, the EOFs could illuminate more of the vertical variability of the tidal signal.

When it comes to the model output, hourly (full and de-tided) files could be used instead. This could for instance improve the resolution of the autocorrelation functions, and possibly resolve more short-lived current events. In general, it should improve how well the model reproduces the data. Furthermore, a model with higher spatial resolution would be advantageous, in particular for areas near the coast, like station 4, see Isachsen (2014).

It would be interesting to find out how much different forcing mechanisms contribute to the flow. In order to do so, it could be useful to run the model several times leaving out different mechanisms, such as the tides or the freshwater input. Temporal correlations between the surface or intermediate flow and e.g. the wind could also be calculated.

Bibliography

Aas, E. (2011). GEF4600 Methods in Physical Oceanography. Compendium.

Albretsen, J. (2011). *NorKyst-800 Report No. 1. User Manual and Technical Descriptions*. Havforskningsinstituttet.

Asplin, L. e. a. (2011). Kystmodellen NorKyst-800 - en strømmodell for hele norskekysten.

Baalsrud, K. and Magnusson, J. (1990). Eutrofisituasjonen i ytre oslofjord. *Hovedrapport. Overvåkingsrapport*, (427/90).

Baalsrud, K. and Magnusson, J. (2002). Indre Oslofjord–natur og miljø. *Fagrådet for vann-og avløpsteknisk samarbeid i indre Oslofjord. Bokbinderiet Johnsen AS, Skien*, page 135.

Beldring, S., Engeland, K., Roald, L. A., Sælthun, N. R., and Voksø, A. (2003). Estimation of parameters in a distributed precipitation-runoff model for norway. *Hydrology and Earth System Sciences Discussions*, 7(3):304–316.

Bjornsson, H. and Venegas, S. (1997). A manual for eof and svd analyses of climatic data. *CCGCR Report*, 97(1).

Braarud, T. and Ruud, J. T. (1937). *The hydrographic conditions and aeration of the Oslo Fjord 1933-1934*. Dybwad in Komm.

Bracco, A., LaCasce, J., and Provenzale, A. (2000). Velocity probability density functions for oceanic floats. *Journal of physical oceanography*, 30(3):461–474.

Broström, G., Carrasco, A., and Berger, S. (2011). Oil drift modelling, the M/V Godafoss accident.

Dahl, F. and Hackett, B. (1988). Eutrofisituasjonen i ytre oslofjord. delrapport 3.4: Data atlas: Strøm-, vær og hydrografiske målinger i faste punkter, mai-november 1988.

Dahl, F., Moen, I., and Skogen, K. (1990). Eutrofisituasjonen i ytre oslofjord 1989. delprosjekt 4.10: Strømmålinger i ytre oslofjord.

Ekman, V. W. (1905). On the influence of the earth's rotation on ocean currents. *Ark. Mat. Astron. Fys.*, 2:1–53.

Gade, H. G. (1968). Horizontal and vertical exchanges and diffusion in the water masses of the Oslo Fjord. *Helgoländer Wissenschaftliche Meeresuntersuchungen*, 17(1-4):462–475.

Grinde, L. (2011). Validation of the numerical ocean weather prediction (nowp) model for the oslofjord, norway, operated by the norwegian meteorological institute.

Hall, M. M. (1986). Horizontal and vertical structure of the gulf stream velocity field at 68 w. *Journal of Physical Oceanography*, 16(11):1814–1828.

Hjort, J. and Gran, H. H. (1900). *Hydrographic-biological Investigations of the Skagerrak and the Christiania Fiord*, volume 1. Oscar Andersen.

Isachsen, P. (2014). Evaluation of two model versions of the Oslofjord with different grid resolutions.

Johannessen, O. M. (1967). Oslofjorden og dens forurensningsproblemer: Del 20 strømkorsundersøkelser i vestfjorden.

Klinck, J. M., O'Brien, J. J., and Svendsen, H. (1981). A simple model of fjord and coastal circulation interaction. *Journal of Physical Oceanography*, 11(12):1612–1626.

Kundu, P. K. (1976). Ekman veering observed near the ocean bottom. *Journal of Physical Oceanography*, 6(2):238–242.

Kutzbach, J. E. (1967). Empirical eigenvectors of sea-level pressure, surface temperature and precipitation complexes over North America. *Journal of Applied Meteorology*, 6(5):791–802.

LaCasce, J. (2005a). Eulerian and lagrangian velocity distributions in the north atlantic. *Journal of physical oceanography*, 35(12):2327–2336.

LaCasce, J. (2005b). Statistics of low frequency currents over the western Norwegian shelf and slope I: current meters. *Ocean Dynamics*, 55(3-4):213–221.

LaCasce, J. (2012). Surface quasigeostrophic solutions and baroclinic modes with exponential stratification. *Journal of Physical Oceanography*, 42(4):569–580.

LaCasce, J. and Engedahl, H. (2005). Statistics of low frequency currents over the western Norwegian shelf and slope II: model. *Ocean Dynamics*, 55(3-4):222–237.

LaCasce, J., Ferrari, R., Marshall, J., Tulloch, R., Balwada, D., and Speer, K. (2014). Float-derived isopycnal diffusivities in the dimes experiment. *Journal of Physical Oceanography*, 44(2):764–780.

Lenn, Y.-D. and Chereskin, T. K. (2009). Observations of ekman currents in the southern ocean. *Journal of Physical Oceanography*, 39(3):768–779.

Lenschow, D., Mann, J., and Kristensen, L. (1994). How long is long enough when measuring fluxes and other turbulence statistics? *Journal of Atmospheric and Oceanic Technology*, 11(3):661–673.

Lilliefors, H. W. (1967). On the kolmogorov-smirnov test for normality with mean and variance unknown. *Journal of the American Statistical Association*, 62(318):399–402.

Moseidjord, H., Svenden, H., Slagstad, D., and Båmstedt, U. (1999). Sensitivity studies of circulation and ocean-shelf exchange off northen norway. *Sarsia*, 84(3-4):191–198.

Pawlowicz, R., Beardsley, B., and Lentz, S. (2002). Classical tidal harmonic analysis including error estimates in MATLAB using T_TIDE. *Computers & Geosciences*, 28(8):929–937.

Pedlosky, J. (1987). An inertial theory of the equatorial undercurrent. *Journal of physical oceanography*, 17(11):1978–1985.

Roberts, J. and Roberts, T. D. (1978). Use of the Butterworth low-pass filter for oceanographic data. *Journal of Geophysical Research: Oceans (1978–2012)*, 83(C11):5510–5514.

Rodhe, J. (1996). On the dynamics of the large-scale circulation of the skagerrak. *Journal of Sea Research*, 35(1):9–21.

Røed, L. and Skåtun, H. (1990). Eutrofisituasjonen i Ytre Oslofjord Delområde 3.3 b: Transportmodell av overflatelaget i Ytre Oslofjord. Rapport 2: Resultater fra simuleringer. En analyse og oppsummering.

Røed, L., Skåtun, H., and Irman-Jacobsen, T. (1990). Eutrofisituasjonen i Ytre Oslofjord 1989. Delprosjekt 4.8: Transportmodell. Simulering av strøm, sporstoffer og partikkelbaner. En analyse og oppsummering.

Shchepetkin, A. F. and McWilliams, J. C. (2005). The regional oceanic modeling system (roms): a split-explicit, free-surface, topography-following-coordinate oceanic model. *Ocean Modelling*, 9(4):347–404.

Skåtun, H. and Røed, L. (1988). Eutrofisituasjonen i Ytre Oslofjord. Delprosjekt 3.3: Transportmodell av overflatelaget i Ytre Oslofjord. Rapport 1: Modellen og dens åpne grensflater.

Smith, P. C. and Schwing, F. B. (1991). Mean circulation and variability on the eastern canadian continental shelf. *Continental Shelf Research*, 11(8):977–1012.

Staalstrøm, A., Aas, E., and Liljebladh, B. (2012). Propagation and dissipation of internal tides in the Oslofjord. *Ocean Science*, 8(4):525.

Staalstrøm, A. and Ghaffari, P. (2014). Field Report from Deployment of Current Meters in Oslofjorden.

Staalstrøm, A. and Ghaffari, P. (2015). Current conditions in the Oslofjord. report draft.

Stigebrandt, A. (1979). Observational evidence for vertical diffusion driven by internal waves of tidal origin in the Oslofjord. *Journal of Physical Oceanography*, 9(2):435–441.

Svendsen, E., Eriksrød, G., and Skogen, M. D. (1995). Numerisk modellering av transport av næringssalter og primærproduksjon i Skagerrak/Kattegat og Ytre Oslofjord.

Thaulow, H. and Faafeng, B. (2014). Indre Oslofjord 2013–status, trusler og tiltak.

Thomson, D. J. (2000). Multitaper analysis of nonstationary and nonlinear time series data. *Nonlinear and nonstationary signal processing*, pages 317–394.

Wåhlin, A. (2002). Topographic steering of dense currents with application to submarine canyons. *Deep Sea Research Part I: Oceanographic Research Papers*, 49(2):305–320.

Welch, P. D. (1967). The use of fast fourier transform for the estimation of power spectra: A method based on time averaging over short, modified periodograms. *IEEE Transactions on audio and electroacoustics*, 15(2):70–73.

Wunsch, C. (1997). The vertical partition of oceanic horizontal kinetic energy. *Journal of Physical Oceanography*, 27(8):1770–1794.